

Axonal transport of autophagosomes is regulated by dynein activators JIP3/JIP4 and ARF/RAB GTPases

Sydney E. Cason^{1,2,3} and Erika L.F. Holzbaur^{1,2,3} *

¹ Department of Physiology, ² Neuroscience Graduate Group, ⁵ Pennsylvania Muscle Institute, University of Pennsylvania

* correspondence to holzbaur@penmedicine.upenn.edu

1 **Abstract**

2 Neuronal autophagosomes, “self-eating” degradative organelles, form at presynaptic sites in the distal
3 axon and are transported to the soma to recycle their cargo. During transit, autophagic vacuoles (AVs)
4 mature through fusion with lysosomes to acquire the enzymes necessary to breakdown their cargo. AV
5 transport is driven primarily by the microtubule motor cytoplasmic dynein in concert with dynactin and a
6 series of activating adaptors that change depending on organelle maturation state. The transport of
7 mature AVs is regulated by the scaffolding proteins JIP3 and JIP4, both of which activate dynein motility
8 in vitro. AV transport is also regulated by ARF6 in a GTP-dependent fashion. While GTP-bound ARF6
9 promotes the formation of the JIP3/4-dynein-dynactin complex, RAB10 competes with the activity of this
10 complex by increasing kinesin recruitment to axonal AVs and lysosomes. These interactions highlight the
11 complex coordination of motors regulating organelle transport in neurons.

12

13 **Summary**

14 Mature autophagosomes in the axon are transported by the microtubule motor dynein, activated by JNK-
15 interacting proteins 3 and 4 (JIP3/4). This motility is regulated by the small GTPases ARF6 and RAB10.
16 The tight regulation of autolysosomal transport is essential for intracellular recycling to maintain neuronal
17 homeostasis.

18 **Introduction**

19 Maintaining neuronal homeostasis across the lifespan requires the continuous turnover of dysfunctional
20 or aged proteins and organelles (Eskelinen, 2019; Kulkarni et al., 2018). Autophagy is a process by which
21 these components can be broken down and recycled (Stavoe and Holzbaur, 2019). Autophagic vacuoles
22 (AVs), the “self-eating” organelle, engulf cargo proteins or organelles in a double-membrane and then
23 fuse with late endosomes and lysosomes (collectively, endolysosomes), which provide the degradative
24 enzymes necessary to breakdown the cargo (Yim and Mizushima, 2020). In neurons, AVs form
25 preferentially at presynaptic sites and at the distal tip of the axon and must be actively transported to the
26 soma, where the majority of protein and organelle biogenesis occurs (Maday et al., 2012; Maday and
27 Holzbaur, 2014; Stavoe et al., 2016; Koltun et al., 2020; Farfel-Becker et al., 2019). The transport of AVs
28 along the axon is primarily driven by the microtubule motor cytoplasmic dynein I, in coordination with its
29 obligate partner complex dynactin (Kimura et al., 2008; Katsumata et al., 2010; Maday et al., 2012). The
30 dynein-dynactin complex needs to be recruited to and activated locally on the AV by adaptor proteins (Fu
31 et al., 2014; Cheng et al., 2015; Khobreakar et al., 2020; Cason et al., 2021). The opposing motor kinesin-
32 1 also localizes to axonal AVs where it may compete with dynein (Wong and Holzbaur, 2014; Maday et
33 al., 2012). Kinesin inactivation on AVs is essential for autophagic transport and flux, and its dysregulation
34 can be observed in the context of neurodegenerative disease (Fu et al., 2014; Boecker et al., 2021; Dou
35 et al., 2022).

36 The simultaneous activation of dynein-dynactin and inactivation of kinesin must therefore
37 be coordinated locally at the AV membrane. This regulation is further complicated by autophagosomal
38 maturation, during which the AV membrane and associated proteins are altered via fusion with
39 endolysosomes (Cason et al., 2021). We previously found that different motor regulatory proteins drive
40 the retrograde transit of AVs along the axon, dependent upon the sub-axonal location and maturation
41 state of the AV (Cason et al., 2021). Specifically, JNK-interacting protein (JIP) 1 regulates the initial transit
42 of nascent AVs in the distal axon by inactivating kinesin-1 (Fu et al., 2014). Huntingtin-associated protein
43 1 (HAP1) activates dynein on partially mature AVs in the mid-axon (Wong and Holzbaur, 2014; Cason et

44 al., 2021). Finally, the motility of the most mature population of axonal AVs is regulated by the motor-
45 interacting protein JIP3 (Cason et al., 2021).

46 Mutations in the JIP3 gene (*MAPK8IP3*; homolog of UNC-16 and Sunday Driver/Syd) result in a
47 rare neurodevelopmental disorder, and JIP3 expression is relatively limited to the brain; in contrast, the
48 related protein JIP4 (*SPAG9*) is expressed ubiquitously (Ito et al., 1999; Jagadish et al., 2005; Kelkar et
49 al., 2000; Platzner et al., 2019). Recent work has shown that JIP3 and JIP4 contain a structurally
50 conserved motif in their N-termini that mediates binding to dynein light intermediate chain (DLIC), a
51 feature common among dynein activating adaptors (Celestino et al., 2022). Further, JIP3/4 can bind to
52 the dynactin subunit p150^{Glued} (Fig. 1 A) and truncated JIP3 can activate dynein motility in a purified
53 system (Montagnac et al., 2009; Rao et al., 2022). However, JIP3 and JIP4 can also interact with the
54 kinesin-1 complex via interactions (Fig. 1 A) with kinesin heavy chain (KIF5) and kinesin light chain (KLC)
55 (Arimoto et al., 2011; Cavalli et al., 2005; Celestino et al., 2022; Cockburn et al., 2018; Montagnac et al.,
56 2009; Sun et al., 2011; Tuvshintugs et al., 2014; Vilela et al., 2019). Further, JIP3 has been reported to
57 induce kinesin activity *in vitro* (Sun et al., 2011; Watt et al., 2015).

58 We therefore asked how JIP3 and JIP4 are regulated to drive the highly processive retrograde
59 transit of AVs along the axon. JIP3 and JIP4 both associate with mature AVs as well as lysosomes, and
60 either full-length protein can activate dynein motility in an *in vitro* assay. We used proteomic databases
61 to identify potential regulators of JIP3/4-dependent motility, and found that the small GTPase ARF6 is
62 enriched in AVs isolated from brain (Goldsmith et al., 2022). In live neurons, we demonstrate that the
63 GTPase state of ARF6 is important for the regulation of both AV and lysosomal motility along axons.
64 Another JIP3/4-interacting GTPase, RAB10, enriched in a lysosomal fraction from brain
65 (Dumrongprechachan et al., 2022), also affected AV and lysosomal motility along axons, but in a distinct
66 fashion. We therefore propose that the recruitment and activation of JIP3/4 at organellar membranes is
67 differentially regulated by discrete small GTPases to generate unique motile behaviors. JIP3/4 represent
68 a growing group of motor-activating proteins that can bind both dynein and kinesin motors on organelle
69 cargos (Arimoto et al., 2011; Bielska et al., 2014; Canty et al., 2021; Cason et al., 2021; Celestino et al.,
70 2022; Colin et al., 2008; Fenton et al., 2021; Fu and Holzbaur, 2013; Kendrick et al., 2019; López-

71 Doménech et al., 2018; Twelvetrees et al., 2019; Vilela et al., 2019; Zhao et al., 2021), and must be tightly
72 regulated by additional binding partners to induce unidirectional transport in the cell.

73

74 **Results**

75 **JIP3 and JIP4 interact with dynein on autolysosomes**

76 Previous studies have implicated both JIP3 and JIP4 in the transport of a number of organelles, especially
77 degradative vesicles such as AVs, endosomes, and lysosomes (Abe et al., 2009; Boecker et al., 2021;
78 Brown et al., 2009; Cason et al., 2021; Choudhary et al., 2017; Drerup and Nechiporuk, 2013; Hill et al.,
79 2019; Kumar et al., 2022; Montagnac et al., 2009; Sun et al., 2017; Willett et al., 2017). Accordingly, both
80 proteins were recently identified via unbiased proteomics as enriched in lysosomal and AV fractions from
81 brain (Fig. 1 B) (Dumrongprechachan et al., 2022; Goldsmith et al., 2022). To assess comigration
82 between JIP3 or JIP4 and both AVs and lysosomes in neurons, we transfected low levels of HaloTag
83 (HT)-JIP3 or JIP4 into primary hippocampal neurons along with mScarlett (mSc)-light chain 3 (LC3)—an
84 autophagosomal marker—and lysosome-associated membrane protein 1 (LAMP1)-mNeonGreen
85 (mNeon). We imaged along the proximal axon, the closest 250 μm to the soma, where we previously
86 observed the strongest impact of JIP3 siRNA on AV motility (Cason et al., 2021). In this region, the vast
87 majority (80-100% depending on LAMP1 expression levels) of LC3 puncta colocalize with LAMP1,
88 indicating at least one fusion event has already occurred (Cason et al., 2022; Boecker et al., 2021; Maday
89 et al., 2012). By contrast, only about a quarter of LAMP1 puncta colocalize with LC3 (Farfel-Becker et
90 al., 2019; Cason et al., 2022). We observed both JIP3 and JIP4 comigrating with LC3 and LAMP1 puncta
91 (Fig. 1, C-D; S1, A-B). While high levels of JIP4 overexpression can disrupt the transport of AVs along
92 the axon (Boecker et al., 2021), we did not observe a change in motility under the conditions tested here
93 (Fig. S1, A-D) due to lower expression levels (see Methods for details). Likewise, overexpression of JIP3
94 or JIP4 did not affect LAMP1+ puncta motility, LC3 or LAMP1 density, nor colocalization between LC3
95 and LAMP1 in the axon (Fig. S1, A-I).

96 Looking specifically at the JIP3 or JIP4 puncta, we noticed that almost all of the motile puncta
97 (moving $\geq 10\mu\text{m}$) were directed retrograde towards the soma (Fig. 1, E-H). Because microtubules in the

98 axon are uniformly polarized with their plus-ends out towards the axon tip and their minus ends pointing
99 towards the soma, the minus-end-directed motor dynein is responsible for retrograde transport (Schroer
100 et al., 1989; Schnapp and Reese, 1989; Heidemann et al., 1981). By contrast, plus-end-directed motors
101 including kinesin-1 are responsible for anterograde transport away from the soma (Vale et al., 1985b; a).
102 Because the vast majority of JIP3 or JIP4 puncta moved retrograde, we therefore asked whether we
103 could observe complex formation between JIP3 or JIP4 and dynein in the axon using proximity ligation
104 assays (PLA). PLA capitalizes on oligonucleotide complementation to identify and label proteins within
105 40 nm of one another in cells (Fig. 1 I) (Alam, 2018). We were indeed able to detect endogenous JIP3 or
106 JIP4 closely apposed to endogenous dynein intermediate chain (DIC) in the axon (Fig. S1, L-M).

107 In live cells, HT-JIP3 or HT-JIP4 colocalized mainly with puncta positive for both LC3 and LAMP1,
108 which can be referred to as mature AVs or autolysosomes. We therefore expressed low levels of HT-LC3
109 then fixed the cells and used antibodies to detect endogenous LAMP1 and assessed colocalization
110 between LC3, LAMP1, and PLA puncta. We observed a striking colocalization between JIP3- or JIP4-
111 DIC PLA puncta and puncta positive for both LC3 and LAMP1, with much less colocalization between
112 PLA puncta and LC3 only or LAMP1 only puncta (Fig. 1, J-M). This finding is consistent with our previous
113 discovery that JIP3 knockdown specifically affected the motility of mature AVs, as compared with other
114 axonal AVs (Cason et al., 2021). Thus, we conclude that JIP3 and JIP4 complex with dynein on mature
115 autolysosomes.

116

117 **JIP3 and JIP4 activate dynein *in vitro***

118 Given that JIP3 and JIP4 can each bind both dynein-dynactin and kinesin-1 (Fig. 1 A), we found it
119 surprising that almost all of the JIP3 or JIP4 puncta in axons moved in the retrograde direction (Fig. 1 H).
120 We therefore asked whether JIP3 or JIP4 preferentially activates dynein or kinesin motors using an *in*
121 *vitro* lysate-based assay with cellular extracts prepared from COS-7 cells (Fig. 2 A). We performed all
122 assays on dynamically growing microtubules; this allowed us to readily differentiate between the faster
123 growing plus-end (Fig. 2 B) and the slower growing minus-end. As positive controls for dynein and kinesin
124 activity respectively, we used BICD2¹⁻⁵⁷² (BICD2N), a truncated form of the known dynein activating

125 adaptor BICD2 that lacks the autoinhibitory domain (Fig. 2, D-F); and KIF5C¹⁻⁵⁶⁰ (K560), the constitutively
126 active truncated version of KIF5C (Fig. S2, A-C). We also co-expressed HA-LIS1 to maximize the
127 assembly of dynein complexes (Elshenawy et al., 2020; Fenton et al., 2021; Htet et al., 2020; Marzo et
128 al., 2020). Note that we used full-length HT-JIP3 or JIP4 in our assays.

129 In the presence of 1mM ATP at a physiological temperature of 37°C, the majority of runs by HT-
130 JIP3- or HT-JIP4-containing motor complexes were towards the minus-end of the microtubule (~90%,
131 Fig. 2 C), with velocities (~2µm/s) and run lengths (~3.2µm) very similar to that of BICD2N (Fig. 2, D-L).
132 The total number of events—both runs ($\geq 0.8\mu\text{m}$ net displacement) and stationary landing events (≤ 0.8
133 s duration with $< 0.8\mu\text{m}$ net displacement)—was also similar among BICD2N (Fig. S2 B), JIP3 (Fig. 2 K),
134 and JIP4 (Fig. 2, E, H, K). Our buffer conditions were sufficient to produce kinesin activity, as assessed
135 using the positive control K560 (Fig. S2, A-C), yet plus-end-directed runs were rare. The few plus-end-
136 directed events we did observe for JIP3- and JIP4-containing complexes moved slightly faster or with
137 shorter run lengths than K560, respectively; however the low n for these observations prevents a direct
138 comparison (Fig. S2, C-E).

139 We were surprised by the low number of plus-end-directed runs, as previous studies have
140 reported kinesin-1 activation by JIP3 and its homolog Sunday driver (Sun et al., 2011; Watt et al., 2015).
141 We tested whether omission of HA-LIS1 would increase the frequency of runs moving toward the
142 microtubule plus-end, but we did not observe more kinesin runs under these conditions (Fig. S2 E). Based
143 upon previous work, we tried combining lysate from cells expressing HT-JIP3 or JIP4 with cells
144 expressing full-length KIF5C-HT (labelled in a different color) and GFP-KLC2. However, these
145 experiments also failed to show substantial transport towards the plus-end of the microtubule (Fig. S2 F).
146 One possible explanation is that previous work did not use polarity-marked microtubules (Sun et al.,
147 2011; Watt et al., 2015); thus, it is possible that the motility they detected was in fact minus-end-directed
148 and dynein-driven. Based upon our data, and consistent with the recent reports on the activation of dynein
149 by JIP3 (Rao et al., 2022; Singh et al., 2022) we conclude that JIP3 and JIP4 robustly activate dynein
150 motility, with only marginal activation of kinesin under the conditions tested. Consistent with these

151 observations, labeled JIP3 and JIP4 both move almost exclusively retrograde in neuronal axons (Fig. 1
152 H).

153

154 **RAB10 overexpression differentially affects the transport of AVs and lysosomes**

155 Many RAB GTPases have been shown to regulate motor complexes at organellar membranes (Guo et
156 al., 2016; Amaya et al., 2016; Horgan et al., 2010; Johansson et al., 2007). In particular, RAB10 was
157 detected in proteomics from brain-derived AVs and lysosomes and is a known JIP3/4 interactor
158 (Waschbüsch et al., 2020; Dumrongprechachan et al., 2022; Goldsmith et al., 2022). To validate this
159 finding, we blotted for RAB10 in fractions from total brain lysate, isolated AVs, and the AV fraction treated
160 with Proteinase K (PK) to digest proteins specifically bound to the outer membrane as described in
161 Goldsmith et al. (2022). RAB10 was not highly enriched in the AV fraction and, additionally, there was no
162 significant difference between RAB10 inside (PK-protected) and outside the AV (Fig. 3 A).

163 Surprisingly, given this lack of enrichment of RAB10 on AVs, when we expressed EGFP-RAB10
164 in hippocampal neurons we noted a potent dominant negative effect on LC3 motility, with EGFP-RAB10
165 expression leading to significantly more stationary/bidirectional AVs as compared with EGFP-tag alone
166 (Tag; Fig. 3, B-C). In the RAB10-expressing condition, examination of RAB10 colocalization revealed
167 that the RAB10+ AVs were almost exclusively stationary, while the few motile AVs did not colocalize with
168 RAB10 (Fig. 3 D). RAB10 expression did not affect LC3 puncta density or colocalization with LAMP1
169 (Fig. S3, A-B).

170 Because the majority (~85%) of the AVs in the proximal axon have fused with a lysosome and
171 are LAMP1+ (Fig. S3 B), we assessed colocalization between EGFP-RAB10, HT-LC3, and endogenous
172 LAMP1 in fixed neurons. We found that RAB10 predominantly colocalized with LAMP1+ organelles,
173 including both autolysosomes and lysosomes (Fig. 3, E-F). Hence, we asked whether LAMP1+ puncta
174 motility is also affected by RAB10 expression. There was no gross effect on LAMP1 puncta motility (Fig.
175 4, A-B). However, when we specifically quantified the motile puncta (moving $\leq 10\mu\text{m}$ in either direction
176 during a 2 min video), we found a significant shift from a mild retrograde bias (~60%) in the GFP
177 expressing cells to a mild anterograde bias (~57%) in the RAB10 expressing cells (Fig. 4 C). Oddly,

178 however, when we examined the LAMP1 puncta colocalized with RAB10, we found the majority to be
179 stationary/bidirectional (Fig. 4 D), like for LC3 (Fig. 3 D). RAB10 expression had no effect on LAMP1
180 colocalization with LC3, but was associated with a mild decrease in LAMP1 puncta in the axon (Fig. S3,
181 C-D).

182 We used PLA (Fig. 1 I) to determine whether the changes in motility were due to a disruption in
183 the formation of JIP3/4-dynein complexes. We found that the number of JIP3/4-DIC PLA puncta did not
184 change upon RAB10 expression (Fig. S3, E-F), nor did the colocalization between JIP3/4-DIC PLA
185 puncta and autophagosomes, autolysosomes, or lysosomes (Fig. S3, G-H). Hence, the decrease in AV
186 motility and the increase in LAMP1 anterograde motility is not due to loss of JIP3/4-dynein complexes.
187 Together, these results suggest that RAB10 can modulate the motility of AVs and lysosomes, potentially
188 by affecting kinesin recruitment and/or activation, rather than by decreasing dynein recruitment or
189 activation.

190

191 **ARF6 GDP-locked mutant disrupts autophagosomal transport**

192 To better understand the regulation of JIP3/4-dependent AV motility, we probed the proteomic data for
193 other possible small GTPases that might affect motor activity or motor coordination. We identified the
194 candidate ARF6, which is present in both the AV and lysosomal proteomic datasets
195 (Dumrongprechachan et al., 2022; Goldsmith et al., 2022) and whose enrichment on the outside of the
196 AV we could validate via immunoblot (Fig. 5 A). ARF6 is a known JIP3/4 interactor and has been
197 previously shown to modulate JIP3/4 motor binding based upon its GTP-binding state: ARF6-GTP
198 increases the binding between JIP3/4 and the dynactin subunit p150^{Glued} (p150) while ARF6-GDP
199 increases binding between JIP3/4 and kinesin light chain (KLC; Fig. 5 B) (Montagnac et al., 2009). Hence,
200 we transfected CFP-ARF6 GTP-locked (Q67L) and GDP-locked (T27N) mutants into our primary
201 hippocampal neurons and assessed the motility of LC3 puncta. While expression of wildtype (ARF6^{WT})
202 and ARF6^{QL} did not have an obvious effect on LC3 motility, ARF6^{TN} expression induced a robust loss of
203 AV motility and a significant increase in the pausing of LC3 puncta (Fig. 5, C-E). However, there was no

204 effect on either LC3 puncta density or AV maturation, measured either by LAMP1 colocalization (Fig. S4,
205 A-B).

206

207 **ARF6 GTP-locked mutant decreases retrograde lysosome pausing**

208 We next assessed motility of LAMP1 puncta in the axon upon ARF6 expression. Here, we observed a
209 very different effect. While gross LAMP1 motility was not significantly different in neurons expressing
210 ARF6^{WT} or ARF6^{TN} expression, expression of the GTP-locked ARF6^{QL} mutant led to a decrease in the
211 stationary/bidirectional fraction of LAMP1 puncta (Fig. 6, A-B). Expression of either locked mutant led to
212 decreased pausing time, although the effect was much bigger in ARF6^{QL}-expressing cells (Fig. 6 C). We
213 evaluated pausing time for LAMP1 puncta colocalized with LC3 (autolysosomes) and those not
214 colocalized (lysosomes) and saw that both organelle subgroups were affected by ARF6^{QL} expression
215 (Fig. 6 D). Neither the LAMP1 puncta colocalized with LC3 nor the LAMP1 density was affected (Fig. S4
216 D-E). However, when we split the LAMP1 puncta into motile fractions, we saw that the pausing effect
217 was limited to the retrograde LAMP1 fraction, with no significant effect on anterograde-moving LAMP1
218 puncta (Fig. 6, E-F). Thus, GTP-bound but not GDP-bound ARF6 increases the efficiency of the dynein
219 complex on LAMP1-positive organelles.

220

221 **ARF6 GTPase status is locally regulated by GAPs and GEFs on the membrane**

222 We next asked whether wildtype ARF6 may be converted locally at AVs and lysosomes into a GTP-
223 bound and GDP-bound state respectively. The nucleotide state of small GTPases is regulated by GTPase
224 activating proteins (GAPs), which induce GTP-to-GDP hydrolysis, and guanine exchange factors (GEFs),
225 which induce release of GDP and binding of a new GTP molecule (Fig. 7 A). There are 10 known ARF6
226 GEFs and 20 GAPs. 60% of ARF6 GEFs and 60% of ARF6 GAPs were detected in lysosomal proteomics
227 (Fig. 7 B) (Dumrongprechachan et al., 2022). Because LC3+ puncta in cells expressing ARF6^{QL} behaved
228 similarly to wildtype-expressing cells, we hypothesized that AVs would be enriched for ARF6 GEFs.
229 Indeed, 50% of ARF6 GEFs and only 20% of ARF6 GAPs were detected in AV proteomics (Fig. 7 B)
230 (Goldsmith et al., 2022). We used immunoblotting to validate the GAPs and GEFs detected in an AV-

231 enriched fraction from brain, and found that the GEFs were highly enriched in the AV fraction and
232 significantly localized to the outer membrane of the AV as judged by protease sensitivity (Fig. 7, C-G).
233 By comparison, the ARF6 GAPs were less enriched and not significantly localized to the outer membrane
234 (Fig. 7, H-J). These observations support a model in which ARF6 GEFs are localized to the AV membrane
235 to locally enrich for ARF6-GTP, which can in turn recruit and/or activate JIP3/4-containing dynein
236 complexes.

237

238 **ARF6 increases the interaction of the JIP3/4-dynein complex with microtubules**

239 Finally, we asked how ARF6 might affect the behavior of JIP3/4-containing motor complexes using *in*
240 *vitro* motility assays. We found that overexpression of GTP-locked ARF6 significantly increased the
241 microtubule landing events of JIP3- or JIP4-containing motor complexes (Fig. 8, A-C), although the
242 frequency of plus- and minus-end-directed events did not change (Fig. 8, D-E). Interestingly, ARF6^{TN}
243 induced the same effect, a significant increase in microtubule-binding events (Fig. S5, A-E). There was
244 no effect on the velocity of motile complexes in either ARF6^{QL} or ARF6^{TN} conditions, but there was a mild
245 reduction in run length upon ARF6 inclusion (~28%; Fig. S5, F-G).

246 Because JIP3 and JIP4 do not directly bind microtubules, the increased landing events must be
247 due to increased interaction with a microtubule-binding protein. The dynactin subunit p150 interacts
248 directly with JIP3/4 and with microtubules via its CAP-Gly domain; additionally, ARF6 binding modulates
249 the interaction between p150 and JIP3/4 (Peris et al., 2006; Ayloo et al., 2014; Moughamian and
250 Holzbaaur, 2012; Montagnac et al., 2009). Finally, p150 binding to the microtubule in the absence of dynein
251 induces statically bound and/or diffusive behaviors (Ayloo et al., 2014; Feng et al., 2020), similar to what
252 we observe. Therefore, we propose that ARF6 increases the efficiency of JIP3/4-containing motor
253 complexes in cells by increasing the microtubule association of JIP3/4 through p150.

254

255 **Discussion**

256 Here, we demonstrate that two related scaffolding proteins, JIP3 and JIP4, both activate dynein *in vitro*,
257 and form a complex with dynein on mature AVs (autolysosomes) in neuronal axons (Fig. 1, 2). We identify

258 two small GTPases that interact with JIP3/4 and affect the axonal transport of AVs and other LAMP1+
259 organelles. RAB10 overexpression halts the retrograde transit of AVs and increases the anterograde bias
260 observed for LAMP1-positive puncta in the axon (Fig. 3, 4). ARF6 also regulates AV motility, in a GTP-
261 binding-dependent fashion: GTP-locked ARF6 decreases the pausing of retrograde-moving LAMP1
262 puncta, while GDP-locked ARF6 increases the fraction of stationary AVs (Fig. 5, 6). Further, ARF6 GEFs
263 are enriched on the outer AV membrane (Fig. 7), meaning ARF6-GTP can be locally upregulated. We
264 propose that locally generated ARF6-GTP recruits the JIP3/4-dynein-dynactin complex and also
265 enhances the association of the complex with microtubules (Fig. 8), leading to more efficient transport of
266 AVs toward the soma.

267 Concurrent with our study, two other groups have shown that purified recombinant truncated JIP3
268 is sufficient to activate dynein-mediated motility *in vitro* (Rao et al., 2022; Singh et al., 2022). Our study
269 adds to this growing body of work, as the approaches used here (1) include endogenous binding partners,
270 which negates the need to use truncated constructs; (2) is performed at physiological temperature on
271 dynamically growing microtubules; and (3) includes competing kinesin complexes. Our average JIP3
272 velocity ($\sim 1.8 \mu\text{m s}^{-1}$) is higher than that observed by the other groups [$0.7 \mu\text{m s}^{-1}$ (Rao et al., 2022); $1 \mu\text{m s}^{-1}$
273 (Singh et al., 2022)], most likely due to the more physiological assay temperature (37°C vs. room
274 temperature). It is, however, consistent with previous observations of dynein activation using lysate
275 assays performed at 37° (Fenton et al., 2021).

276 Previous work has reported that the *Drosophila* JIP3 ortholog Sunday driver (*syd*) activates
277 kinesin-1 (Sun et al., 2011). However, these assays were performed using mammalian cell lysate at room
278 temperature on stabilized microtubules without polarity labelling, and the average velocities ($0.6\text{-}1.0 \mu\text{m s}^{-1}$)
279 and run lengths ($3\text{-}5.5 \mu\text{m}$) observed suggest that minus end-directed motility may have dominated in
280 their assays, as these values are more consistent with dynein-mediated transport (Olenick et al., 2016;
281 Urnavicius et al., 2018; Fenton et al., 2021; Canty et al., 2021; Fu et al., 2014; Fu and Holzbaur, 2013;
282 Rao et al., 2022; Singh et al., 2022; Sun et al., 2011). Similar assays performed with mammalian JIP3
283 (Watt et al., 2015) resulted in velocities ($\sim 0.25 \mu\text{m s}^{-1}$) more consistent with kinesin-1 activation; however,
284 the relatively short run lengths ($\sim 0.75 \mu\text{m}$) suggest that JIP3 may require additional effectors to fully

285 activate kinesin-1 motility. Consistent with this conclusion, binding assays suggest that JIP3 and the
286 unrelated motor effector protein JNK-interacting protein 1 (JIP1) cooperatively activate kinesin-1 (Sun et
287 al., 2017). JIP1 alone is unlikely to be sufficient for kinesin-1 activation (Blasius et al., 2007; Sun et al.,
288 2017), but in single molecule assays using cell lysates, JIP1 overexpression increases the number of
289 kinesin-1-driven motility events (Fu and Holzbaur, 2013; Fu et al., 2014). Binding assays suggest that
290 the binding of JIP1 to KHC and KLC, concurrent with the binding of JIP3 to KLC, is necessary to fully
291 relieve kinesin-1 autoinhibition (Sun et al., 2017). Further, overexpression of either JIP1 or JIP3 leads to
292 the accumulation of the other adaptor at microtubule plus-ends in cells, suggesting cotransport with
293 kinesin (Hammond et al., 2008). While JIP3 does not oligomerize with JIP4, JIP1 and JIP3 interact both
294 directly and indirectly through KLC, where they bind distinct residues in the tetratricopeptide repeat (TPR)
295 domain (Hammond et al., 2008; Kelkar et al., 2005). Of note, JIP1 and JIP3 have been implicated in the
296 anterograde transport of many of the same organelles, including synaptic vesicle proteins, TrkB receptor,
297 amyloid precursor protein (APP), mitochondria, and signaling proteins such as JNK (Choudhary et al.,
298 2017; Horiuchi et al., 2005; Sun et al., 2017; Fu and Holzbaur, 2013; Drerup and Nechiporuk, 2013; Sato
299 et al., 2015), further supporting a cooperative interaction between these motor activators.

300 Notably, both JIP1 and JIP3/4 have been previously implicated in the transport of RAB10+
301 vesicles (Kluss et al., 2022; Bonet-Ponce et al., 2020; Deng et al., 2014). In our study, RAB10 appears
302 to increase the recruitment and/or activation of kinesin on LC3+ and LAMP1+ puncta. RAB10, like many
303 other RABs, is regulated by phosphorylation with phospho-RAB10 (especially T73) being generally more
304 active and membrane-associated (Yan et al., 2018; Lara Ordóñez et al., 2022; Kluss et al., 2022; Wauters
305 et al., 2020; Waschbüsch et al., 2020; Homma et al., 2021). RAB10, especially phospho-RAB10,
306 regulates the motility of multiple kinesin-1 and kinesin-3 cargoes within cells (Etoh and Fukuda, 2019;
307 Deng et al., 2014; Taylor et al., 2015; Zajac and Horne-Badovinac, 2022). RAB10 can directly complex
308 with kinesin-3 (KIF13) and regulate its activity (Etoh and Fukuda, 2019; Zajac and Horne-Badovinac,
309 2022). However, its interaction with kinesin-1 (KIF5) must be mediated by adaptor proteins. We therefore
310 propose an integrated model (Fig. 9 A) in which JIP3 or JIP4, together with JIP1, mediate the anterograde
311 transport of RAB10+ cargo, including some populations of lysosomes. Phospho-RAB10 recruits JIP3/4

312 and JIP1 to LAMP1+ organelles; upon RAB10 binding, JIP3/4 and JIP1 bind to kinesin-1 to induce the
313 anterograde transit of the organelle (Fig. 3, 4). RAB10 can also directly bind kinesin-3 to induce
314 anterograde transport, circumventing the JIP3/4-JIP1 complex.

315 RAB10 is a known target of the kinase LRRK2, which is hyperactive in some genetic forms of
316 Parkinson's disease (Yan et al., 2018; Wauters et al., 2020; Bonet-Ponce et al., 2020). Our group
317 previously showed that hyperactive, disease-associated LRRK2 increased the level of phospho-RABs
318 and kinesin present on the outer membrane of AVs (Boecker et al., 2021). Additionally, hyperactive
319 LRRK2 increased the recruitment of JIP4 and, to a lesser degree, JIP3 to the AV membrane (Boecker et
320 al., 2021). We therefore hypothesize that phospho-RAB10 forms a complex with JIP4 to recruit and
321 activate kinesin (Fig. 9 B). If exogenously expressed at high levels, JIP4 can block AV motility (Boecker
322 et al., 2021), but when expressed at more modest levels, JIP4 comigrates with autolysosomes (Fig. S2),
323 like JIP3. It is unknown whether JIP4 can also interact with JIP1 to activate kinesin-1. However, based
324 upon our work and others, we suggest that JIP3 and JIP4 are functionally redundant with their primary
325 difference being expression in different tissues (Gowrishankar et al., 2021; Tuvshintugs et al., 2014; Sato
326 et al., 2015). Thus, in non-neuronal cells where JIP3 is not expressed, JIP4 may replace JIP3 in the
327 kinesin activation complex.

328 JIP3 and JIP4 can also induce retrograde transport of LAMP1+ organelles, including
329 autolysosomes. ARF6 was previously shown to block JIP3 or JIP4 binding to kinesin, possibly through
330 steric hindrance: the KLC and ARF6 binding sites are highly overlapping (Vilela et al., 2019; Cockburn et
331 al., 2018; Hammond et al., 2008; Llinas et al., 2016; Isabet et al., 2009; Montagnac et al., 2009) (Fig. 1
332 B). Instead, ARF6 enhances the interaction between JIP3/4 and the dynactin subunit p150^{Glued}
333 (Montagnac et al., 2009). The increased frequency of microtubule landing events for JIP3/4—in the
334 absence of changes to other motility parameters—induced by addition of ARF6 to our *in vitro* assays
335 (Fig. 8) is consistent with an increased interaction with p150^{Glued}, which contains a microtubule-binding
336 domain but no motor activity (Ayloo et al., 2014; Feng et al., 2020). Microtubule binding, especially
337 through dynactin and general dynein effectors like CLIP-170, has previously been shown to be important
338 for dynein recruitment and initiation of motility (Moughamian and Holzbaur, 2012; Moughamian et al.,

339 2013; Nirschl et al., 2016; McKenney et al., 2016). Stepwise recruitment of dynactin and then dynein to
340 the microtubule has not previously been shown for cargo-specific activating activators for dynein.
341 However, the JIP3/4-related dynein effector Rab7-interacting protein (RILP) was previously shown to
342 bind to dynactin prior to the initiation of dynein activity, suggesting a similar mechanism (Johansson et
343 al., 2007). While RILP has not yet been shown to activate motor activity *in vitro*, its N-terminus—including
344 the motor binding domains—is very similar to that of JIP3 and JIP4 (Celestino et al., 2022; Vilela et al.,
345 2019; Matsui et al., 2012). We therefore hypothesize that the formation of an initial microtubule-bound
346 cargo-binding protein-dynein activator-dynactin complex, such as the ARF6-JIP3/4-dynactin complex, is
347 a common mechanism in the initiation of dynein-mediated transport of diverse cargos.

348 In single molecule motility assays, we observed no difference between GTP- and GDP-locked
349 ARF6 (Fig. 8, S9). However, in neurons, expression of GTP- and GDP-locked ARF6 induced significant
350 changes in organelle transport (Fig. 5, 6). We hypothesize that this difference may be due to a key role
351 for bound nucleotide in regulating the membrane association of ARF6. ARF6 contains a myristoyl anchor
352 and binds more tightly to membranes in its GTP-bound state than in its GDP-bound state (Ménétrety et
353 al., 2000; Duellberg et al., 2021). In our *in vitro* assays, membranes are first removed via centrifugation
354 of cell lysates, making this assay less sensitive to effects of the nucleotide state of ARF6. Therefore, we
355 propose that the differential effects observed in cells and *in vitro* when comparing GTP- and GDP-locked
356 ARF6 are likely due to increased membrane interaction and the subsequent stepwise recruitment of JIP3
357 or JIP4, dynactin, and dynein (Fig. 9 A).

358 Interestingly, overexpression of GTP-locked ARF6 is sufficient to ameliorate the AV motility
359 phenotype observed in hyperactive LRRK2 mutant conditions (Dou et al., 2022). Under increased LRRK2
360 activity, JIP3/4 seem to exhibit enhanced interaction with kinesin and phosphorylated RABs (Dou et al.,
361 2022; Boecker et al., 2021; Kluss et al., 2022; Bonet-Ponce et al., 2020). In these conditions, GTP-locked
362 ARF6 expression presumably scaffolds the formation of more JIP3/4-dynein-dynactin complexes to
363 compete with the RAB-JIP3/4-kinesin-1 complexes (Dou et al., 2022). ARF6 and phospho-RAB10 (or
364 RAB35) may compete to bind the same limited pool of JIP3/4, or excess JIP3/4 may be available for
365 recruitment into multiple motor complexes concurrently (Bonet-Ponce et al., 2020; Miyamoto et al., 2014;

366 Kobayashi and Fukuda, 2012). While ARF6 and RAB10 bind different regions of JIP3/4, the ARF6 binding
367 site and the KLC binding site are mutually exclusive (Isabet et al., 2009); thus it is likely that these are
368 two completely discrete complexes.

369 It is possible that crosstalk occurs locally between ARF6 GAPs and GEFs and RAB kinases and
370 phosphatases to prevent local activation of both dynein and kinesin, which would result in non-processive
371 tug-of-war. For example, the RAB10/RAB35 effector ACAP2 is known to also function as a GAP for ARF6
372 (Shi and Grant, 2013; Shi et al., 2012; Kobayashi and Fukuda, 2012; Miyamoto et al., 2014). ACAP2 is
373 present in both the AV and lysosome proteomics datasets from brain (Goldsmith et al., 2022;
374 Dumrongprechachan et al., 2022); however, we found that ACAP2 was primarily an AV cargo, not on the
375 outer membrane, consistent with local enrichment for ARF6-GTP on the AV membrane. However,
376 ACAP2 enrichment on lysosomes may locally promote GTP hydrolysis by ARF6, leading to dissociation
377 of the GTPase from the membrane. Interestingly, analysis of the RAB35-ACAP2 structure indicates that
378 ACAP2 specifically binds to the LRRK2 phosphorylation site within RAB35 (Lin et al., 2019). Thus, LRRK2
379 kinase activity may locally enhance the formation of RAB-JIP3/4-kinesin-1 complexes, and also prevent
380 local accumulation of ARF6-GTP and the resultant activation of dynein-dynactin activity on lysosomes.

381 Hyperphosphorylated RAB10 is induced by Parkinson's disease-causing mutations in LRRK2,
382 and is also a hallmark pathological feature of Alzheimer's disease (Yan et al., 2018). Mutations in the
383 JIP1-JIP3 cargo APP cause familial Alzheimer's disease; further, both axonal transport and autophagy
384 are disrupted in a multitude of neurodegenerative diseases (Wong and Holzbaur, 2015; Kins et al., 2006;
385 Guillaud et al., 2020; Goldstein, 2012). Mutations in JIP3 cause a rare neurodevelopmental disorder
386 (Platzer et al., 2019) and double-knockout of JIP3 and JIP4 leads to robust neurodegeneration (Sato et
387 al., 2015; Gowrishankar et al., 2021). Additionally, ARF6 knockout in neurons leads to defects in axonal
388 development (Akiyama et al., 2014). Because these proteins and the processes they regulate are all
389 dysfunctional in neurodevelopmental and/or neurodegenerative disease, it is essential that we continue
390 to tease apart the detailed mechanisms involved in order to better inform therapy development.

391

392 **Acknowledgements**

393 This research was supported by NIH grant R35 GM126950 to E.L.F.H. The authors declare no competing
394 financial interests. We gratefully acknowledge Mariko Tokito for her tireless cloning, Dan Dou and Alex
395 Boecker for discussions, and Juliet Goldsmith for her generosity with autophagosome fractionation
396 samples.

397 **Materials and methods**

398 **Plasmids and reagents**

399 Constructs, all of which were verified by DNA sequencing, include the following:

| Construct | Source |
|-------------------------|---|
| CFP-ARF6 WT, QL, and TN | Gift from J. Swanson (Addgene # 11382, 11386, 11387) |
| BICD2N-Halo | Full-length mouse BICD2 in the pEGFP vector (gift from A. Akhmanova, Utrecht University) was used to generate a truncated construct spanning residues 1–572 fused to the HaloTag and cloned into pcDNA3.1 |
| Halo-JIP3 (EGFP vector) | HaloTag fused to the N-terminus of hJIP3 from cDNA Clone (GE: MGC9053013) fused in pEGFP vector backbone |
| Halo-JIP4 (CMV vector) | Subcloned from pGEXP1-JIP4 #DU27651, acquired from MRC PPU Reagents and services, University of Dundee |
| Halo-JIP3 (CMV vector) | Halo-JIP3 sequence (from EGFP vector construct) subcloned into (Halo-JIP4) CMV vector |
| Halo-JIP4 (EGFP vector) | Halo-JIP4 sequence (from CMV vector construct) subcloned into (Halo-JIP3) EGFP vector |
| K560-Halo | First 560 aa of human KIF5B from pET17: K560 GFP ST (gift from R. Vale, University of California San Francisco) subcloned into pHTC-HaloTag CMVneo vector (Promega) |
| KIF5C-Halo | Full-length mouse kinesin-1 heavy chain (KIF5C) in pRK5 myc plasmid (gift from J. Kittler, University of Surrey) with HaloTag fused to C-terminus |
| GFP-KLC2 | Full-length WT mouse KLC2 in CB6 driven expression vector |
| LAMP1-mNEON | Gift from D. Gadella (Addgene plasmid # 98882). |
| mCherry-EGFP-LC3B | Gift from T. Johansen, University of Troms |
| mScarlet-LC3B | Subcloned from Addgene #21073 and Addgene #85054 |
| HA-LIS1 | Gift from D. Smith, University of South Carolina |
| EGFP-RAB10 | Gift from M. Scidmore (Addgene plasmid # 49472) |

400

401 We previously used a HT-JIP4 construct in a CMVNeo backbone that expressed in cells at extremely
402 high levels (Fig. S1, J-K). We subcloned the HT-JIP4 into an EGFP backbone (the EGFP was previously
403 removed via subcloning), which we were already using for our HT-JIP3. This new HT-JIP4 expresses at
404 more modest levels and does not affect AV or LAMP1 motility (Fig. S1, A-E). Therefore, we report that
405 our previous finding was an overexpression artifact. In all neuronal experiments, we used the EGFP
406 backbone JIP3/4; in the TIRF assays, we used the CMV backbone JIP3/4.

407

408 Antibodies include the following:

| Antibody | Source | Dilution |
|-------------------------|-------------------------|-----------------|
| anti- ACAP2/CENTB2 | ThermoFisher, PA5-18209 | WB 1:1000 |
| anti- ARF6 | Cell Signaling, D12G6 | WB 1:800 |
| anti- CYTH (pan) | ThermoFisher, MA1-062 | WB 1:1000 |
| anti- DIC | EMD Millipore, MAB1618 | PLA@1:200 |
| anti- GIT1 | Biorbyt, orb99082 | WB 1:1000 |
| anti- Halo (polyclonal) | Promega, G9281 | WB 1:500 |
| anti- Halo (monoclonal) | Promega, G9211 | WB 1:500 |
| anti- IQSEC1/BRAG2 | ThermoFisher, PA5-38019 | WB 1:500 |
| anti- IQSEC2/BRAG1 | ThermoFisher, PA5-72831 | WB 1:500 |
| anti- IQSEC3/BRAG3 | Biorbyt, orb317640 | WB 1:500 |
| anti- JIP3/MAPK8IP3 | Abcam, ab196761 | PLA 1:25 |
| anti- JIP4/SPAG9 | Cell Signaling, 5519 | PLA 1:25 |
| anti- LAMP1 | R&D Systems, AF4800 | IF 1:50 |
| anti- RAB10 | Abcam, ab237703 | WB 1:500 |
| anti- SMAP2 | Biorbyt, orb1142130 | WB 1:2000 |
| anti-Sheep (2°) 405 | Abcam, ab175676 | IF 1:1000 |
| anti-Sheep (2°) 647 | Abcam, ab150179 | IF 1:1000 |

409

410 **Primary hippocampal culture**

411 Sprague Dawley rat hippocampal neurons at embryonic day 18 were obtained from the Neurons R Us
412 Culture Service Center at the University of Pennsylvania. Cells (proximity ligation assay, 40,000 cells on
413 7mm glass; live imaging, 200,000 cells on 20 mm glass) were plated in glass-bottom 35 mm dishes
414 (MatTek) that were precoated with 0.5 mg/ml poly-L-lysine (Sigma Aldrich). Cells were initially plated in
415 Attachment Media (MEM supplemented with 10% horse serum, 33 mM D-glucose, and 1 mM sodium
416 pyruvate) which was replaced with Maintenance Media (Neurobasal [Gibco] supplemented with 33 mM
417 D-glucose, 2 mM GlutaMAX (Invitrogen), 100 units/ml penicillin, 100 mg/ml streptomycin, and 2% B-27
418 [ThermoFisher]) after 5-20 h. Neurons were maintained at 37 C in a 5% CO2 incubator; cytosine
419 arabinoside (Ara-C; final conc. 1 μ M) was added the day after plating to prevent glia cell proliferation. For
420 transfections, neurons (7-10 DIV) were transfected with 0.35–1.5 μ g of total plasmid DNA using
421 Lipofectamine 2000 Transfection Reagent (ThermoFisher, 11668030) and incubated for 18-48 h.

422

423 **Live neuron imaging and analysis**

424 Neurons were imaged in Imaging Media (HibernateE [Brain Bits] supplemented with 2% B27 and 33 mM
425 D-glucose). Autophagosome (1-1.3 frames/sec) and lysosome (0.5-0.65 frames/sec) behavior was
426 monitored in the proximal axon (<200 μm from the soma) of 8-12 DIV neurons for 2-3 min. Neurons were
427 imaged in an environmental chamber at 37°C on a Perkin Elmer UltraView Vox spinning disk confocal
428 on a Nikon Eclipse Ti Microscope with an Apochromat 100 x 1.49 numerical aperture (NA) oil-immersion
429 objective and a Hamamatsu EMCCD C9100-50 camera driven by Volocity (PerkinElmer). Only cells
430 expressing moderate levels of fluorescent proteins were imaged to avoid overexpression artifacts or
431 aggregation. It should be noted that the quality of the primary neuron dissections affected
432 autophagosomal motility, but compared conditions were always collected from the same dissections
433 and imaging sessions.

434 Kymographs were generated in ImageJ (<https://imagej.net/ImageJ2>) using the MultiKymograph
435 plugin (line width, 1-5) and analyzed in ImageJ. Puncta were classified as either anterograde (moving
436 $\geq 10\mu\text{m}$ towards the axon tip), retrograde (moving $\geq 10\mu\text{m}$ towards the soma), or stationary/bidirectional
437 (net movement $< 10\mu\text{m}$ during the video). Because fluorescent LC3 is cytosolic (as well as punctate) and
438 neurites occasionally crossed in culture, raw videos were referenced throughout kymograph analysis to
439 ensure only real puncta (≥ 1.5 SD from the axon mean) were included in analyses. All comigration
440 analyses were performed using kymographs.

441

442 **Proximity ligation assay**

443 Neurons were transfected (Lipofectamine 2000) with 0.3 μg EGFP plasmid (for GFP fill) and 0.5 μg Halo-
444 tagged effector following above protocol then 24 h later (DIV 7–8) fixed in PBS containing 4%
445 paraformaldehyde and 4% sucrose for 8 min. Duolink™ In Situ PLA Mouse/Rabbit kit with red detection
446 reagents (Sigma-Aldrich, DUO92101-1KT) was used according to manufacturer's protocol. We used
447 dynein intermediate chain antibody (Mouse MAB1618) plus JIP3 antibody (Rabbit ab196761), JIP4
448 antibody (Rabbit Cell Signalling, 5519), or no second 1° antibody (negative control). Both 2° antibodies
449 (Mouse and Rabbit) were added for all experiments (including negative control). Z-stacks (0.25 μm steps)
450 were acquired on an inverted epifluorescence microscope (DMI6000B; Leica) with an Apochromat 63 x

451 1.4 NA oil-immersion objective and a charge-coupled device camera (ORCA-R2; Hamamatsu Photonics)
452 using LAS-AF software (Leica). Puncta were counted manually using ImageJ.

453

454 **Cell line culture**

455 COS-7 (ATCC) cells were maintained in DMEM (Corning) supplemented with 1% GlutaMAX and 10%
456 FBS. Cells were maintained at 37 C in a 5% CO₂ incubator. For motility assays and co-
457 immunoprecipitation experiments, COS-7 cells were plated on 10 cm plates and transfected 24h prior to
458 lysis using FuGENE 6 (Promega; 6-12 µg total DNA). Cells were routinely tested for mycoplasma using
459 a MycoAlert detection kit (Lonza, LT07). COS-7 cells were authenticated by ATCC.

460

461 **Motility assay**

462 The movement of JIP3-, JIP4-, BICD2N-, or K560-containing complexes from cell extracts was tracked
463 using TIRF microscopy. Motility assays were performed in flow chambers constructed with a glass slide
464 and a coverslip silanized with PlusOne Repel-Silane ES (GE Healthcare), held together with vacuum
465 grease to form a ~10 µl chamber. Rigor kinesin-1E236A (0.5 µM) was non-specifically absorbed to the
466 coverslip 73 and the chamber was then blocked with 5% pluronic F-127 (Sigma-Aldrich). 250 nM
467 GMPCPP microtubule (MT) seeds, labeled at a 1:40 ratio with HiLyte Fluor 488 tubulin (Cytoskeleton,
468 Denver, CO), were flowed into the chamber and immobilized by interaction with rigor kinesin-1E236A.
469 11.25 µM free tubulin (labeled at a 1:20 ratio with HiLyte Fluor 488 tubulin) was added with the lysate to
470 grow dynamic microtubules from the seeds. COS-7 cells grown in 10 cm plates to 70–80% confluence
471 expressing full-length Halo-tagged HAP1, BICD2N or HaloTag alone were labeled with TMR 18–24 h
472 post-transfection then lysed in 100 µl lysis buffer [40 mM Hepes (pH 7.4), 120 mM NaCl, 1 mM EDTA, 1
473 mM ATP, 0.1% Triton X-100, 1 mM PMSF, 0.01 mg ml⁻¹ TAME, 0.01 mg ml⁻¹ leupeptin, and 1 µg ml⁻¹
474 pepstatin-A]. Cell lysates were clarified by centrifugation (17,000g) and diluted in P12 motility buffer [12
475 mM Pipes (pH 6.8), 1 mM EGTA, and 2 mM MgCl₂] supplemented with 1 mM Mg-ATP, 1 mM GTP, 0.08
476 mg ml⁻¹ casein, 0.08 mg ml⁻¹ bovine serum albumin, 2.55 mM DTT, 0.05% methylcellulose, and an
477 oxygen scavenging system (0.5 mg ml⁻¹ glucose oxidase, 470 U ml⁻¹ catalase, and 3.8 mg ml⁻¹ glucose).

478 All the videos (2 min, 4-5 frames s⁻¹) were acquired at 37°C using a Nikon TIRF microscopy system
479 (Perkin Elmer, Waltham, MA) on an inverted Ti microscope equipped with a 100× objective and an
480 ImageEM C9100-13 camera (Hamamatsu Photonics, Hamamatsu, Japan) with a pixel size of 0.158 μm
481 and controlled with the program Volocity (Improvision, Coventry, England).

482

483 **Motility assay analysis**

484 At least 5 microtubules per video were analyzed by generating kymographs using the MultiKymograph
485 plugin of ImageJ and analyzed in Excel (Microsoft, Redmond, WA). MY polarity was determined one of
486 two ways. (1) MT were imaged at 10 sec intervals during the entire acquisition (2 min). (2) MT were
487 imaged for 30 sec at 4-5 frames sec⁻¹ before and after motor imaging. In this case, only MT present in
488 both the before and after videos were analyzed. The MT length (to which the number of events was
489 normalized) was either (1) the final length at the end of the entire (2 min) acquisition; or (2) the initial
490 length at the beginning of the “after” video, respectively. In either case, only non-bundled MT that could
491 be clearly seen both growing and catastrophing regularly were analyzed.

492 At least 5 microtubules were analyzed per replicate; 3 biological and technical replicates were
493 performed for a final n = 20 microtubules per condition. Kymographs were generated using the
494 MultiKymograph plugin (line width, 1) in ImageJ (<https://imagej.net/ImageJ2>). Analysis was performed
495 using KymoButler 74 with manual post-hoc curation, as described here. To be classified as an event, the
496 duration must be greater than 0.8 seconds or the run length greater than 1.6 μm, and at least 1.5 SD
497 above the local background (surrounding ~100 μm²). To be classified as plus-end- or minus-end-directed
498 run, the punctum must travel greater than 5 pixels (0.8 μm) in that direction.

499

500 **Autophagosome fractionation**

501 Enriched autophagosome fractions were isolated from mouse brain via sequential ultracentrifugation,
502 adding Gly-Phe-β-naphthylamide to inactivate and deplete lysosomal vesicles and thus enhance the
503 integrity of autophagosome-associated proteins 75; detailed protocols and validations can be found in
504 60. Briefly, brains were collected from wildtype mice on the C57BL/6J background (Ref 14699058) and

505 homogenized in a tissue grinder in an ice cold buffered 10mM Hepes, 1mM EDTA, 250 mM sucrose
506 solution, then subjected to three differential centrifugations through Nycodenz and Percoll discontinuous
507 gradients to isolate vesicles of the appropriate size and density. The autophagosome enriched fraction
508 was then divided and either immediately lysed for the identification of all internal and externally-
509 associated proteins on autophagosomes (A fraction), treated with 10 µg proteinase-K for 45min at 37°C
510 to degrade externally associated proteins and enrich for membrane-protected autophagosome cargo (P
511 fraction), or membrane permeabilized by the addition of 0.2% triton x-100 prior to proteinase K treatment
512 to confirm proteinase K efficacy (T fraction). The lysis buffer used contained a final concentration of 0.5%
513 NP-40 with 1x protease and phosphatase inhibitors, PMSF and Pepstatin A. Protein concentration was
514 measured by Bradford assay and equal amounts of protein in denaturing buffer were run on SDS-PAGE
515 gels.

516

517 **Immunoblotting**

518 For fluorescence Western blotting, samples were analyzed by SDS- PAGE and transferred onto PDVF
519 Immobilon FL (Millipore). Membranes were dried for at least 1 h, rehydrated in methanol, and stained for
520 total protein (LI-COR REVERT Total Protein Stain). Following imaging of the total protein, membranes
521 were destained, blocked for 5min in EveryBlot Blocking Buffer (BioRad #12010021), and incubated
522 overnight at 4°C with primary antibodies diluted in EveryBlot Blocking Buffer. Membranes were washed
523 four times for 5 min in 1xTBS Washing Solution (50 mM Tris-HCl pH 7.4, 274 mM NaCl, 9 mM KCl, 0.1%
524 Tween-20), incubated in secondary antibodies diluted in EveryBlot Blocking Buffer with 0.01% SDS for 1
525 hr, and again washed four times for 5 min in the washing solution. Membranes were immediately imaged
526 using an Odyssey CLx Infrared Imaging System (LI-COR). Band intensity was measured in the LI-COR
527 Image Studio application.

528

529 **Analysis of organelle enrichment publications**

530 Goldsmith et al., (2022) and Dumrongprechachan et al., (2022) performed AV and lysosomal
531 enrichments, respectively, and performed mass spectrometry on the resultant proteins to determine

532 proteins associated with the organelles. To compare these datasets, which pulled down different amounts
533 of total protein, we normalized the number of peptides from each to the average number of peptides
534 detected for ARF-related proteins (normalization factor) in each preparation. The number of peptides for
535 each detected protein was divided by the normalization factor (13.5 for lysosomes, 2.6 for AVs). Note
536 that for the AVs, we used the number of peptides in the fraction not treated with proteinase K (AV fraction).

537

538 **Statistics**

539 All statistical analyses were performed in Prism (GraphPad, San Diego, CA). Bars represent mean \pm
540 S.E.M. unless otherwise indicated. n indicates the number of events or cells pooled across at least 3
541 trials per experiment. Parametric or nonparametric tests were used where appropriate, but formal testing
542 was not performed. Statistical measures are described in the legends.

543

544 **Author contributions**

545 Sydney E. Cason, Conceptualization, Resources, Data curation, Formal analysis, Validation,
546 Investigation, Visualization, Methodology, Project administration, Writing—original draft and
547 review/editing; Erika L.F. Holzbaaur, Conceptualization, Supervision, Funding acquisition, Project
548 administration, Writing—review/editing

549 **References**

- 550 Abe, N., A. Almenar-Queralt, C. Lillo, Z. Shen, J. Lozach, S.P. Briggs, D.S. Williams, L.S.B. Goldstein, and V.
551 Cavalli. 2009. Sunday Driver Interacts with Two Distinct Classes of Axonal Organelles. *J. Biol. Chem.*
552 284:34628–34639. doi:10.1074/jbc.M109.035022.
- 553 Akiyama, M., H. Hasegawa, T. Hongu, M.A. Frohman, A. Harada, H. Sakagami, and Y. Kanaho. 2014. Trans-
554 regulation of oligodendrocyte myelination by neurons through small GTPase Arf6-regulated secretion of
555 fibroblast growth factor-2. *Nat Commun.* 5:4744. doi:10.1038/ncomms5744.
- 556 Alam, M.S. 2018. Proximity Ligation Assay. *Current Protocols in Immunology*.
- 557 Amaya, C., R.D. Militello, S.D. Calligaris, and M.I. Colombo. 2016. Rab24 interacts with the Rab7/Rab interacting
558 lysosomal protein complex to regulate endosomal degradation. *Traffic.* 17:1181–1196.
559 doi:10.1111/tra.12431.
- 560 Arimoto, M., S.P. Koushika, B.C. Choudhary, C. Li, K. Matsumoto, and N. Hisamoto. 2011. The Caenorhabditis
561 elegans JIP3 Protein UNC-16 Functions As an Adaptor to Link Kinesin-1 with Cytoplasmic Dynein. *J.*
562 *Neurosci.* 31:2216–2224. doi:10.1523/JNEUROSCI.2653-10.2011.
- 563 Ayloo, S., J.E. Lazarus, A. Dodda, M. Tokito, E.M. Ostap, and E.L.F. Holzbaur. 2014. Dynactin functions as both a
564 dynamic tether and brake during dynein-driven motility. *Nat Commun.* 5:4807. doi:10.1038/ncomms5807.
- 565 Bielska, E., M. Schuster, Y. Roger, A. Berepiki, D.M. Soanes, N.J. Talbot, and G. Steinberg. 2014. Hook is an
566 adapter that coordinates kinesin-3 and dynein cargo attachment on early endosomes. *The Journal of Cell*
567 *Biology.* 204:989–1007. doi:10.1083/jcb.201309022.
- 568 Boecker, C.A., J. Goldsmith, D. Dou, G.G. Cajka, and E.L.F. Holzbaur. 2021. Increased LRRK2 kinase activity
569 alters neuronal autophagy by disrupting the axonal transport of autophagosomes. *Current Biology.*
570 doi:10.1016/j.cub.2021.02.061.
- 571 Bonet-Ponce, L., A. Beilina, C.D. Williamson, E. Lindberg, J.H. Kluss, S. Saez-Atienzar, N. Landeck, R. Kumaran,
572 A. Mamais, C.K.E. Bleck, Y. Li, and M.R. Cookson. 2020. LRRK2 mediates tubulation and vesicle sorting
573 from lysosomes. *Sci Adv.* 6. doi:10.1126/sciadv.abb2454.
- 574 Brown, H.M., H.A.V. Epps, A. Goncharov, B.D. Grant, and Y. Jin. 2009. The JIP3 scaffold protein UNC-16 regulates
575 RAB-5 dependent membrane trafficking at C. elegans synapses. *Developmental Neurobiology.* 69:174–
576 190. doi:10.1002/dneu.20690.
- 577 Canty, J.T., A. Hensley, and A. Yildiz. 2021. TRAK adaptors coordinate the recruitment and activation of dynein
578 and kinesin to control mitochondrial transport. 2021.07.30.454553. doi:10.1101/2021.07.30.454553.

- 579 Cason, S.E., P.J. Carman, C. Van Duyne, J. Goldsmith, R. Dominguez, and E.L.F. Holzbaur. 2021. Sequential
580 dynein effectors regulate axonal autophagosome motility in a maturation-dependent pathway. *Journal of*
581 *Cell Biology*. 220:e202010179. doi:10.1083/jcb.202010179.
- 582 Cason, S.E., S.S. Mogre, E.L.F. Holzbaur, and E.F. Koslover. 2022. Spatiotemporal analysis of axonal
583 autophagosome–lysosome dynamics reveals limited fusion events and slow maturation. *MBoC*. 33:ar123.
584 doi:10.1091/mbc.E22-03-0111.
- 585 Cavalli, V., P. Kujala, J. Klumperman, and L.S.B. Goldstein. 2005. Sunday Driver links axonal transport to damage
586 signaling. *J. Cell Biol.* 168:775–787. doi:10.1083/jcb.200410136.
- 587 Celestino, R., J.B. Gama, A.F. Castro-Rodrigues, D.J. Barbosa, H. Rocha, E.A. d’Amico, A. Musacchio, A.X.
588 Carvalho, J.H. Morais-Cabral, and R. Gassmann. 2022. JIP3 interacts with dynein and kinesin-1 to regulate
589 bidirectional organelle transport. *Journal of Cell Biology*. 221:e202110057. doi:10.1083/jcb.202110057.
- 590 Cheng, X.-T., B. Zhou, M.-Y. Lin, Q. Cai, and Z.-H. Sheng. 2015. Axonal autophagosomes recruit dynein for
591 retrograde transport through fusion with late endosomes. *J Cell Biol.* 209:377–386.
592 doi:10.1083/jcb.201412046.
- 593 Choudhary, B., M. Kamak, N. Ratnakaran, J. Kumar, A. Awasthi, C. Li, K. Nguyen, K. Matsumoto, N. Hisamoto,
594 and S.P. Koushika. 2017. UNC-16/JIP3 regulates early events in synaptic vesicle protein trafficking via
595 LRK-1/LRRK2 and AP complexes. *PLOS Genetics*. 13:e1007100. doi:10.1371/journal.pgen.1007100.
- 596 Cockburn, J.J.B., S.J. Hesketh, P. Mulhair, M. Thomsen, M.J. O’Connell, and M. Way. 2018. Insights into Kinesin-
597 1 Activation from the Crystal Structure of KLC2 Bound to JIP3. *Structure*. 26:1486-1498.e6.
598 doi:10.1016/j.str.2018.07.011.
- 599 Colin, E., D. Zala, G. Liot, H. Rangone, M. Borrell-Pagès, X.-J. Li, F. Saudou, and S. Humbert. 2008. Huntingtin
600 phosphorylation acts as a molecular switch for anterograde/retrograde transport in neurons. *EMBO J*.
601 27:2124–2134. doi:10.1038/emboj.2008.133.
- 602 Deng, C.-Y., W.-L. Lei, X.-H. Xu, X.-C. Ju, Y. Liu, and Z.-G. Luo. 2014. JIP1 Mediates Anterograde Transport of
603 Rab10 Cargos during Neuronal Polarization. *J. Neurosci*. 34:1710–1723. doi:10.1523/JNEUROSCI.4496-
604 13.2014.
- 605 Dou, D., E.M. Smith, C.S. Evans, C.A. Boecker, and E.L.F. Holzbaur. 2022. Regulatory imbalance between LRRK2
606 kinase, PPM1H phosphatase, and ARF6 GTPase disrupts the axonal transport of autophagosomes.
607 2022.11.14.516471. doi:10.1101/2022.11.14.516471.

- 608 Drerup, C.M., and A.V. Nechiporuk. 2013. JNK-Interacting Protein 3 Mediates the Retrograde Transport of Activated
609 c-Jun N-Terminal Kinase and Lysosomes. *PLOS Genetics*. 9:e1003303.
610 doi:10.1371/journal.pgen.1003303.
- 611 Duellberg, C., A. Auer, N. Canigova, K. Loibl, and M. Loose. 2021. In vitro reconstitution reveals phosphoinositides
612 as cargo-release factors and activators of the ARF6 GAP ADAP1. *PNAS*. 118.
613 doi:10.1073/pnas.2010054118.
- 614 Dumrongprechachan, V., R.B. Salisbury, L. Butler, M.L. MacDonald, and Y. Kozorovitskiy. 2022. Dynamic
615 proteomic and phosphoproteomic atlas of corticostriatal axons in neurodevelopment. *eLife*. 11:e78847.
616 doi:10.7554/eLife.78847.
- 617 Elshenawy, M.M., E. Kusakci, S. Volz, J. Baumbach, S.L. Bullock, and A. Yildiz. 2020. Lis1 activates dynein motility
618 by modulating its pairing with dynactin. *Nature Cell Biology*. 22:570–578. doi:10.1038/s41556-020-0501-4.
- 619 Eskelinen, E.-L. 2019. Autophagy: Supporting cellular and organismal homeostasis by self-eating. *The International
620 Journal of Biochemistry & Cell Biology*. 111:1–10. doi:10.1016/j.biocel.2019.03.010.
- 621 Etoh, K., and M. Fukuda. 2019. Rab10 regulates tubular endosome formation through KIF13A and KIF13B motors.
622 *Journal of Cell Science*. 132:jcs226977. doi:10.1242/jcs.226977.
- 623 Farfel-Becker, T., J.C. Roney, X.-T. Cheng, S. Li, S.R. Cuddy, and Z.-H. Sheng. 2019. Neuronal Soma-Derived
624 Degradative Lysosomes Are Continuously Delivered to Distal Axons to Maintain Local Degradation
625 Capacity. *Cell Reports*. 28:51-64.e4. doi:10.1016/j.celrep.2019.06.013.
- 626 Feng, Q., A.M. Gicking, and W.O. Hancock. 2020. Dynactin p150 promotes processive motility of DDB complexes
627 by minimizing diffusional behavior of dynein. *MBoC*. 31:782–792. doi:10.1091/mbc.E19-09-0495.
- 628 Fenton, A.R., T.A. Jongens, and E.L.F. Holzbaur. 2021. Mitochondrial adaptor TRAK2 activates and functionally
629 links opposing kinesin and dynein motors. *Nat Commun*. 12:4578. doi:10.1038/s41467-021-24862-7.
- 630 Fu, M., and E.L.F. Holzbaur. 2013. JIP1 regulates the directionality of APP axonal transport by coordinating kinesin
631 and dynein motors. *J Cell Biol*. 202:495–508. doi:10.1083/jcb.201302078.
- 632 Fu, M., J.J. Nirschl, and E.L.F. Holzbaur. 2014. LC3 Binding to the Scaffolding Protein JIP1 Regulates Processive
633 Dynein-Driven Transport of Autophagosomes. *Dev Cell*. 29:577–590. doi:10.1016/j.devcel.2014.04.015.
- 634 Goldsmith, J., A. Ordureau, J.W. Harper, and E.L.F. Holzbaur. 2022. Brain-derived autophagosome profiling reveals
635 the engulfment of nucleoid-enriched mitochondrial fragments by basal autophagy in neurons. *Neuron*.
636 doi:10.1016/j.neuron.2021.12.029.

- 637 Goldstein, L.S.B. 2012. Axonal transport and neurodegenerative disease: Can we see the elephant? *Prog*
638 *Neurobiol.* 99. doi:10.1016/j.pneurobio.2012.03.006.
- 639 Gowrishankar, S., L. Lyons, N.M. Rafiq, A. Roczniak-Ferguson, P. De Camilli, and S.M. Ferguson. 2021.
640 Overlapping roles of JIP3 and JIP4 in promoting axonal transport of lysosomes in human iPSC-derived
641 neurons. *MBoC.* mbc.E20-06-0382. doi:10.1091/mbc.E20-06-0382.
- 642 Guillaud, L., S.E. El-Agamy, M. Otsuki, and M. Terenzio. 2020. Anterograde Axonal Transport in Neuronal
643 Homeostasis and Disease. *Front Mol Neurosci.* 13:556175. doi:10.3389/fnmol.2020.556175.
- 644 Guo, X., G.G. Fariás, R. Mattera, and J.S. Bonifacino. 2016. Rab5 and its effector FHF contribute to neuronal
645 polarity through dynein-dependent retrieval of somatodendritic proteins from the axon. *Proc Natl Acad Sci*
646 *U S A.* 113:E5318-5327. doi:10.1073/pnas.1601844113.
- 647 Hammond, J.W., K. Griffin, G.T. Jih, J. Stuckey, and K.J. Verhey. 2008. Co-operative Versus Independent Transport
648 of Different Cargoes by Kinesin-1. *Traffic.* 9:725–741. doi:10.1111/j.1600-0854.2008.00722.x.
- 649 Heidemann, S.R., J.M. Landers, and M.A. Hamborg. 1981. Polarity orientation of axonal microtubules. *J Cell Biol.*
650 91:661–665. doi:10.1083/jcb.91.3.661.
- 651 Hill, S.E., K.J. Kauffman, M. Krout, J.E. Richmond, T.J. Melia, and D.A. Colón-Ramos. 2019. Maturation and
652 Clearance of Autophagosomes in Neurons Depends on a Specific Cysteine Protease Isoform, ATG-4.2.
653 *Developmental Cell.* 49:251-266.e8. doi:10.1016/j.devcel.2019.02.013.
- 654 Homma, Y., S. Hiragi, and M. Fukuda. 2021. Rab family of small GTPases: an updated view on their regulation and
655 functions. *The FEBS Journal.* 288:36–55. doi:10.1111/febs.15453.
- 656 Horgan, C.P., S.R. Hanscom, R.S. Jolly, C.E. Futter, and M.W. McCaffrey. 2010. Rab11-FIP3 links the Rab11
657 GTPase and cytoplasmic dynein to mediate transport to the endosomal-recycling compartment. *Journal of*
658 *Cell Science.* 123:181–191. doi:10.1242/jcs.052670.
- 659 Horiuchi, D., R.V. Barkus, A.D. Pilling, A. Gassman, and W.M. Saxton. 2005. APLIP1, a Kinesin Binding JIP-1/JNK
660 Scaffold Protein, Influences the Axonal Transport of Both Vesicles and Mitochondria in *Drosophila*. *Current*
661 *Biology.* 15:2137–2141. doi:10.1016/j.cub.2005.10.047.
- 662 Htet, Z.M., J.P. Gillies, R.W. Baker, A.E. Leschziner, M.E. DeSantis, and S.L. Reck-Peterson. 2020. LIS1 promotes
663 the formation of activated cytoplasmic dynein-1 complexes. *Nature Cell Biology.* 22:518–525.
664 doi:10.1038/s41556-020-0506-z.

- 665 Isabet, T., G. Montagnac, K. Regazzoni, B. Raynal, F. El Khadali, P. England, M. Franco, P. Chavrier, A. Houdusse,
666 and J. Ménétreay. 2009. The structural basis of Arf effector specificity: the crystal structure of ARF6 in a
667 complex with JIP4. *EMBO J.* 28:2835–2845. doi:10.1038/emboj.2009.209.
- 668 Ito, M., K. Yoshioka, M. Akechi, S. Yamashita, N. Takamatsu, K. Sugiyama, M. Hibi, Y. Nakabeppu, T. Shiba, and
669 K.-I. Yamamoto. 1999. JSAP1, a Novel Jun N-Terminal Protein Kinase (JNK)-Binding Protein That
670 Functions as a Scaffold Factor in the JNK Signaling Pathway. *Molecular and Cellular Biology.* 19:7539–
671 7548. doi:10.1128/MCB.19.11.7539.
- 672 Jagadish, N., R. Rana, R. Selvi, D. Mishra, M. Garg, S. Yadav, J.C. Herr, K. Okumura, A. Hasegawa, K. Koyama,
673 and A. Suri. 2005. Characterization of a novel human sperm-associated antigen 9 (SPAG9) having
674 structural homology with c-Jun N-terminal kinase-interacting protein. *Biochemical Journal.* 389:73–82.
675 doi:10.1042/BJ20041577.
- 676 Johansson, M., N. Rocha, W. Zwart, I. Jordens, L. Janssen, C. Kuijl, V.M. Olkkonen, and J. Neefjes. 2007. Activation
677 of endosomal dynein motors by stepwise assembly of Rab7–RILP–p150Glued, ORP1L, and the receptor
678 β III spectrin. *Journal of Cell Biology.* 176:459–471. doi:10.1083/jcb.200606077.
- 679 Katsumata, K., J. Nishiyama, T. Inoue, N. Mizushima, J. Takeda, and M. Yuzaki. 2010. Dynein- and activity-
680 dependent retrograde transport of autophagosomes in neuronal axons. *Autophagy.* 6:378–385.
681 doi:10.4161/auto.6.3.11262.
- 682 Kelkar, N., S. Gupta, M. Dickens, and R.J. Davis. 2000. Interaction of a Mitogen-Activated Protein Kinase Signaling
683 Module with the Neuronal Protein JIP3. *Molecular and Cellular Biology.* 20:1030–1043.
684 doi:10.1128/MCB.20.3.1030-1043.2000.
- 685 Kelkar, N., C.L. Standen, and R.J. Davis. 2005. Role of the JIP4 Scaffold Protein in the Regulation of Mitogen-
686 Activated Protein Kinase Signaling Pathways. *Molecular and Cellular Biology.* 25:2733–2743.
687 doi:10.1128/MCB.25.7.2733-2743.2005.
- 688 Kendrick, A.A., A.M. Dickey, W.B. Redwine, P.T. Tran, L.P. Vaites, M. Dzieciatkowska, J.W. Harper, and S.L. Reck-
689 Peterson. 2019. Hook3 is a scaffold for the opposite-polarity microtubule-based motors cytoplasmic dynein-
690 1 and KIF1C. *Journal of Cell Biology.* 218:2982–3001. doi:10.1083/jcb.201812170.
- 691 Khobreakar, N.V., S. Quintremil, T.J. Dantas, and R.B. Vallee. 2020. The Dynein Adaptor RILP Controls Neuronal
692 Autophagosome Biogenesis, Transport, and Clearance. *Developmental Cell.*
693 doi:10.1016/j.devcel.2020.03.011.

- 694 Kimura, S., T. Noda, and T. Yoshimori. 2008. Dynein-dependent Movement of Autophagosomes Mediates Efficient
695 Encounters with Lysosomes. *Cell Structure and Function*. 33:109–122. doi:10.1247/csf.08005.
- 696 Kins, S., N. Lauther, A. Szodorai, and K. Beyreuther. 2006. Subcellular trafficking of the amyloid precursor protein
697 gene family and its pathogenic role in Alzheimer's disease. *Neurodegenerative Diseases*. 3:218–26.
698 doi:10.1159/000095259.
- 699 Kluss, J.H., A. Beilina, C.D. Williamson, P.A. Lewis, M.R. Cookson, and L. Bonet-Ponce. 2022. Lysosomal
700 positioning regulates Rab10 phosphorylation at LRRK2+ lysosomes. *Proceedings of the National Academy
701 of Sciences*. 119:e2205492119. doi:10.1073/pnas.2205492119.
- 702 Kobayashi, H., and M. Fukuda. 2012. Rab35 regulates Arf6 activity through centaurin- β 2 (ACAP2) during neurite
703 outgrowth. *J Cell Sci*. 125:2235–2243. doi:10.1242/jcs.098657.
- 704 Koltun, B., S. Ironi, N. Gershoni-Emek, I. Barrera, M. Hleihil, S. Nanguneri, R. Sasmal, S.S. Agasti, D. Nair, and K.
705 Rosenblum. 2020. Measuring mRNA translation in neuronal processes and somata by tRNA-FRET. *Nucleic
706 Acids Research*. 48:e32. doi:10.1093/nar/gkaa042.
- 707 Kulkarni, A., J. Chen, and S. Maday. 2018. Neuronal autophagy and intercellular regulation of homeostasis in the
708 brain. *Current Opinion in Neurobiology*. 51:29–36. doi:10.1016/j.conb.2018.02.008.
- 709 Kumar, G., P. Chawla, N. Dhiman, S. Chadha, S. Sharma, K. Sethi, M. Sharma, and A. Tuli. 2022. RUFY3 links
710 Arl8b and JIP4-Dynein complex to regulate lysosome size and positioning. *Nat Commun*. 13:1540.
711 doi:10.1038/s41467-022-29077-y.
- 712 Lara Ordóñez, A.J., R. Fasiczka, B. Fernández, Y. Naaldijk, E. Fdez, M. Blanca Ramírez, S. Phan, D. Boassa, and
713 S. Hilfiker. 2022. The LRRK2 signaling network converges on a centriolar phospho-Rab10/RILPL1 complex
714 to cause deficits in centrosome cohesion and cell polarization. *Biology Open*. 11:bio059468.
715 doi:10.1242/bio.059468.
- 716 Lin, L., Y. Shi, M. Wang, C. Wang, J. Zhu, and R. Zhang. 2019. Rab35/ACAP2 and Rab35/RUSC2 Complex
717 Structures Reveal Molecular Basis for Effector Recognition by Rab35 GTPase. *Structure*. 27:729-740.e3.
718 doi:10.1016/j.str.2019.02.008.
- 719 Llinas, P., M. Chenon, T.Q. Nguyen, C. Moreira, A. de Régibus, A. Coquard, M.J. Ramos, R. Guérois, P.A.
720 Fernandes, and J. Ménétrey. 2016. Structure of a truncated form of leucine zipper II of JIP3 reveals an
721 unexpected antiparallel coiled-coil arrangement. *Acta Cryst F*. 72:198–206.
722 doi:10.1107/S2053230X16001576.

- 723 López-Doménech, G., C. Covill-Cooke, D. Ivankovic, E.F. Halff, D.F. Sheehan, R. Norkett, N. Birsa, and J.T. Kittler.
724 2018. Miro proteins coordinate microtubule- and actin-dependent mitochondrial transport and distribution.
725 *EMBO J.* 37:321–336. doi:10.15252/embj.201696380.
- 726 Maday, S., and E.L.F. Holzbaur. 2014. Autophagosome biogenesis in primary neurons follows an ordered and
727 spatially regulated pathway. *Dev Cell.* 30:71–85. doi:10.1016/j.devcel.2014.06.001.
- 728 Maday, S., K.E. Wallace, and E.L.F. Holzbaur. 2012. Autophagosomes initiate distally and mature during transport
729 toward the cell soma in primary neurons. *J Cell Biol.* 196:407–417. doi:10.1083/jcb.201106120.
- 730 Marzo, M.G., J.M. Griswold, and S.M. Markus. 2020. Pac1/LIS1 stabilizes an uninhibited conformation of dynein to
731 coordinate its localization and activity. *Nature Cell Biology.* 22:559–569. doi:10.1038/s41556-020-0492-1.
- 732 Matsui, T., N. Ohbayashi, and M. Fukuda. 2012. The Rab interacting lysosomal protein (RILP) homology domain
733 functions as a novel effector domain for small GTPase Rab36: Rab36 regulates retrograde melanosome
734 transport in melanocytes. *J. Biol. Chem.* 287:28619–28631. doi:10.1074/jbc.M112.370544.
- 735 McKenney, R.J., W. Huynh, R.D. Vale, and M. Sirajuddin. 2016. Tyrosination of α -tubulin controls the initiation of
736 processive dynein–dynactin motility. *The EMBO Journal.* 35:1175–1185. doi:10.15252/embj.201593071.
- 737 Ménétrey, J., E. Macia, S. Pasqualato, M. Franco, and J. Cherfils. 2000. Structure of Arf6–GDP suggests a basis
738 for guanine nucleotide exchange factors specificity. *Nat Struct Mol Biol.* 7:466–469. doi:10.1038/75863.
- 739 Miyamoto, Y., N. Yamamori, T. Torii, A. Tanoue, and J. Yamauchi. 2014. Rab35, acting through ACAP2 switching
740 off Arf6, negatively regulates oligodendrocyte differentiation and myelination. *Mol Biol Cell.* 25:1532–1542.
741 doi:10.1091/mbc.E13-10-0600.
- 742 Montagnac, G., J.-B. Sibarita, S. Loubéry, L. Daviet, M. Romao, G. Raposo, and P. Chavrier. 2009. ARF6 Interacts
743 with JIP4 to Control a Motor Switch Mechanism Regulating Endosome Traffic in Cytokinesis. *Current*
744 *Biology.* 19:184–195. doi:10.1016/j.cub.2008.12.043.
- 745 Moughamian, A.J., and E.L.F. Holzbaur. 2012. Dynactin Is Required for Transport Initiation from the Distal Axon.
746 *Neuron.* 74:331–343. doi:10.1016/j.neuron.2012.02.025.
- 747 Moughamian, A.J., G.E. Osborn, J.E. Lazarus, S. Maday, and E.L.F. Holzbaur. 2013. Ordered Recruitment of
748 Dynactin to the Microtubule Plus-End is Required for Efficient Initiation of Retrograde Axonal Transport. *J.*
749 *Neurosci.* 33:13190–13203. doi:10.1523/JNEUROSCI.0935-13.2013.
- 750 Nirschl, J.J., M.M. Magiera, J.E. Lazarus, C. Janke, and E.L.F. Holzbaur. 2016. α -Tubulin Tyrosination and CLIP-
751 170 Phosphorylation Regulate the Initiation of Dynein-Driven Transport in Neurons. *Cell Reports.* 14:2637–
752 2652. doi:10.1016/j.celrep.2016.02.046.

- 753 Olenick, M.A., M. Tokito, M. Boczkowska, R. Dominguez, and E.L.F. Holzbaur. 2016. Hook Adaptors Induce
754 Unidirectional Processive Motility by Enhancing the Dynein-Dynactin Interaction. *J. Biol. Chem.* 291:18239–
755 18251. doi:10.1074/jbc.M116.738211.
- 756 Peris, L., M. Thery, J. Fauré, Y. Saoudi, L. Lafanechère, J.K. Chilton, P. Gordon-Weeks, N. Galjart, M. Bornens, L.
757 Wordeman, J. Wehland, A. Andrieux, and D. Job. 2006. Tubulin tyrosination is a major factor affecting the
758 recruitment of CAP-Gly proteins at microtubule plus ends. *J Cell Biol.* 174:839–849.
759 doi:10.1083/jcb.200512058.
- 760 Platzer, K., H. Sticht, S.L. Edwards, W. Allen, K.M. Angione, M.T. Bonati, C. Brasington, M.T. Cho, L.A. Demmer,
761 T. Falik-Zaccai, C.N. Gamble, Y. Hellenbroich, M. Iascone, F. Kok, S. Mahida, H. Mandel, T. Marquardt, K.
762 McWalter, B. Panis, A. Pepler, H. Pinz, L. Ramos, D.N. Shinde, C. Smith-Hicks, A.P.A. Stegmann, P. Stöbe,
763 C.T.R.M. Stumpel, C. Wilson, J.R. Lemke, N. Di Donato, K.G. Miller, and R. Jamra. 2019. De Novo Variants
764 in MAPK8IP3 Cause Intellectual Disability with Variable Brain Anomalies. *The American Journal of Human*
765 *Genetics.* 104:203–212. doi:10.1016/j.ajhg.2018.12.008.
- 766 Rao, L., P. Li, X. Liu, Q. Wang, A.I. Son, A. Gennerich, J. Shih-Hwa Liu, and X. Fu. 2022. Doublecortin and JIP3
767 are neural-specific counteracting regulators of dynein-mediated retrograde trafficking. *eLife.* 11:e82218.
768 doi:10.7554/eLife.82218.
- 769 Sato, T., M. Ishikawa, M. Mochizuki, M. Ohta, M. Ohkura, J. Nakai, N. Takamatsu, and K. Yoshioka. 2015.
770 JSAP1/JIP3 and JLP regulate kinesin-1-dependent axonal transport to prevent neuronal degeneration. *Cell*
771 *Death Differ.* 22:1260–1274. doi:10.1038/cdd.2014.207.
- 772 Schnapp, B.J., and T.S. Reese. 1989. Dynein is the motor for retrograde axonal transport of organelles. *PNAS.*
773 86:1548–1552. doi:10.1073/pnas.86.5.1548.
- 774 Schroer, T.A., E.R. Steuer, and M.P. Sheetz. 1989. Cytoplasmic dynein is a minus end-directed motor for
775 membranous organelles. *Cell.* 56:937–946. doi:10.1016/0092-8674(89)90627-2.
- 776 Shi, A., and B.D. Grant. 2013. Interactions between Rab and Arf GTPases regulate endosomal phosphatidylinositol-
777 4,5-bisphosphate during endocytic recycling. *Small GTPases.* 4:106–109. doi:10.4161/sgtp.23477.
- 778 Shi, A., O. Liu, S. Koenig, R. Banerjee, C.C.-H. Chen, S. Eimer, and B.D. Grant. 2012. RAB-10-GTPase-mediated
779 regulation of endosomal phosphatidylinositol-4,5-bisphosphate. *PNAS.* 109:E2306–E2315.
780 doi:10.1073/pnas.1205278109.
- 781 Singh, K., C.K. Lau, J.B. Gama, R. Gassmann, and A.P. Carter. 2022. The lysosomal adaptor JIP3 activates dynein-
782 dynactin via a short coiled coil. 2022.08.17.504273. doi:10.1101/2022.08.17.504273.

- 783 Stavoe, A.K.H., S.E. Hill, D.H. Hall, and D.A. Colón-Ramos. 2016. KIF1A/UNC-104 transports ATG-9 to regulate
784 neurodevelopment and autophagy at synapses. *Dev Cell*. 38:171–185. doi:10.1016/j.devcel.2016.06.012.
- 785 Stavoe, A.K.H., and E.L.F. Holzbaur. 2019. Autophagy in Neurons. *Annu Rev Cell Dev Biol*. 35:477–500.
786 doi:10.1146/annurev-cellbio-100818-125242.
- 787 Sun, F., C. Zhu, R. Dixit, and V. Cavalli. 2011. Sunday Driver/JIP3 binds kinesin heavy chain directly and enhances
788 its motility. *EMBO J*. 30:3416–3429. doi:10.1038/emboj.2011.229.
- 789 Sun, T., Y. Li, T. Li, H. Ma, Y. Guo, X. Jiang, M. Hou, S. Huang, and Z. Chen. 2017. JIP1 and JIP3 cooperate to
790 mediate TrkB anterograde axonal transport by activating kinesin-1. *Cell. Mol. Life Sci*. 74:4027–4044.
791 doi:10.1007/s00018-017-2568-z.
- 792 Taylor, C.A., J. Yan, A.S. Howell, X. Dong, and K. Shen. 2015. RAB-10 Regulates Dendritic Branching by Balancing
793 Dendritic Transport. *PLOS Genetics*. 11:e1005695. doi:10.1371/journal.pgen.1005695.
- 794 Tuvshintugs, B., T. Sato, R. Enkhtuya, K. Yamashita, and K. Yoshioka. 2014. JSAP1 and JLP are required for ARF6
795 localization to the midbody in cytokinesis. *Genes to Cells*. 19:692–703. doi:10.1111/gtc.12170.
- 796 Twelvetrees, A.E., F. Lesept, E.L.F. Holzbaur, and J.T. Kittler. 2019. The adaptor proteins HAP1a and GRIP1
797 collaborate to activate the kinesin-1 isoform KIF5C. *J Cell Sci*. 132. doi:10.1242/jcs.215822.
- 798 Urnavicius, L., C.K. Lau, M.M. Elshenawy, E. Morales-Rios, C. Motz, A. Yildiz, and A.P. Carter. 2018. Cryo-EM
799 shows how dynactin recruits two dyneins for faster movement. *Nature*. 554:202–206.
800 doi:10.1038/nature25462.
- 801 Vale, R.D., T.S. Reese, and M.P. Sheetz. 1985a. Identification of a Novel Force-Generating Protein, Kinesin,
802 Involved in Microtubule-Based Motility. *Cell*. 42:39–50.
- 803 Vale, R.D., B.J. Schnapp, T. Mitchison, E. Steuer, T.S. Reese, and M.P. Sheetz. 1985b. Different axoplasmic
804 proteins generate movement in opposite directions along microtubules in vitro. *Cell*. 43:623–632.
805 doi:10.1016/0092-8674(85)90234-X.
- 806 Vilela, F., C. Velours, M. Chenon, M. Aumont-Nicaise, V. Campanacci, A. Thureau, O. Pylypenko, J. Andreani, P.
807 Llinas, and J. Ménétreay. 2019. Structural characterization of the RH1-LZI tandem of JIP3/4 highlights RH1
808 domains as a cytoskeletal motor-binding motif. *Sci Rep*. 9:1–15. doi:10.1038/s41598-019-52537-3.
- 809 Waschbüsch, D., E. Purlyte, P. Pal, E. McGrath, D.R. Alessi, and A.R. Khan. 2020. Structural Basis for Rab8a
810 Recruitment of RILPL2 via LRRK2 Phosphorylation of Switch 2. *Structure*. 28:406–417.e6.
811 doi:10.1016/j.str.2020.01.005.

- 812 Watt, D., R. Dixit, and V. Cavalli. 2015. JIP3 Activates Kinesin-1 Motility to Promote Axon Elongation. *J Biol Chem.*
813 290:15512–15525. doi:10.1074/jbc.M115.651885.
- 814 Wauters, F., T. Cornelissen, D. Imberechts, S. Martin, B. Koentjoro, C. Sue, P. Vangheluwe, and W. Vandenberghe.
815 2020. LRRK2 mutations impair depolarization-induced mitophagy through inhibition of mitochondrial
816 accumulation of RAB10. *null*. 16:203–222. doi:10.1080/15548627.2019.1603548.
- 817 Willett, R., J.A. Martina, J.P. Zewe, R. Wills, G.R.V. Hammond, and R. Puertollano. 2017. TFEB regulates lysosomal
818 positioning by modulating TMEM55B expression and JIP4 recruitment to lysosomes. *Nat Commun.* 8:1580.
819 doi:10.1038/s41467-017-01871-z.
- 820 Wong, Y.C., and E.L.F. Holzbaur. 2014. The Regulation of Autophagosome Dynamics by Huntingtin and HAP1 Is
821 Disrupted by Expression of Mutant Huntingtin, Leading to Defective Cargo Degradation. *J. Neurosci.*
822 34:1293–1305. doi:10.1523/JNEUROSCI.1870-13.2014.
- 823 Wong, Y.C., and E.L.F. Holzbaur. 2015. Autophagosome dynamics in neurodegeneration at a glance. *J. Cell. Sci.*
824 128:1259–1267. doi:10.1242/jcs.161216.
- 825 Yan, T., L. Wang, J. Gao, S.L. Siedlak, M.L. Huntley, P. Termsarasab, G. Perry, S.G. Chen, and X. Wang. 2018.
826 Rab10 Phosphorylation is a Prominent Pathological Feature in Alzheimer’s Disease. *J Alzheimers Dis.*
827 63:157–165. doi:10.3233/JAD-180023.
- 828 Yim, W.W.-Y., and N. Mizushima. 2020. Lysosome biology in autophagy. *Cell Discovery.* 6:1–12.
829 doi:10.1038/s41421-020-0141-7.
- 830 Zajac, A.L., and S. Horne-Badovinac. 2022. Kinesin-directed secretion of basement membrane proteins to a
831 subdomain of the basolateral surface in *Drosophila* epithelial cells. *Current Biology.* 32:735-748.e10.
832 doi:10.1016/j.cub.2021.12.025.
- 833 Zhao, Y., E. Song, W. Wang, C.-H. Hsieh, X. Wang, W. Feng, X. Wang, and K. Shen. 2021. Metaxins are core
834 components of mitochondrial transport adaptor complexes. *Nat Commun.* 12:83. doi:10.1038/s41467-020-
835 20346-2.
- 836
- 837

838 **Legends**

839 **Figure 1. JIP3/4 comigrate with and interact with dynein on autolysosomes. (A)** N-terminal region
840 of JIP3 and JIP4, scaled to the primary sequence. Arrows: green, JIP-DIC PLA only; magenta, LC3 only;
841 cyan, LAMP1 only; ochre, LC3 + LAMP1; white, LC3 + LAMP1 + JIP-DIC PLA. **(B)** Relative enrichment
842 (normalized number of peptides, see Methods for details) for JIP3 (Mapk8ip3) and JIP4 (Spag9) in the
843 proteomics performed by Goldsmith et al., (2022) and Dumrongprechachan et al., (2022). **(C-D)** Time
844 series demonstrating JIP3 and JIP4 comigration with LC3 (AV marker) and LAMP1 (lysosome marker).
845 **(E-F)** Example kymographs from the proximal axons of neurons transfected with JIP3 or JIP4.
846 Kymographs depict distance on the x-axis and time on the y-axis. Annotated kymographs (annot.) mirror
847 the above kymographs with the JIP3/4+ puncta paths pseudo-colored for visualization. **(G)** Quantification
848 of JIP3/4+ puncta moving retrograde ($\geq 10\mu\text{m}$ towards the soma), anterograde ($\geq 10\mu\text{m}$ towards the axon
849 tip), or exhibiting bidirectional/stationary motility (moving $< 10\mu\text{m}$). n = 10 neurons; two-way ANOVA with
850 Sidak's multiple comparisons test (anterograde, P = 0.8976; stationary/bidirectional, P = 0.0767;
851 retrograde, P = 0.2792). **(H)** Fraction of motile events ($\geq 10\mu\text{m}$ either direction) moving retrograde. n =
852 10 neurons; unpaired t test (P = 0.9776). **(I)** Schematic illustrating the proximity ligation assay (PLA). **(J-**
853 **M)** Example micrographs and quantifications showing colocalization between LC3, LAMP1, and JIP3-
854 DIC (J-K) or JIP4-DIC (L-M) puncta. n = 20 neurons; one-way ANOVA with Tukey's multiple comparisons
855 test; JIP3 (LC3 v. LC3 + LAMP1, P < 0.0001; LC3 v. LAMP1, P = 0.7236; LAMP1 v. LC3 + LAMP1, P <
856 0.0001); JIP4 (LC3 v. LC3 + LAMP1, P < 0.0001; LC3 v. LAMP1, P = 0.9879; LAMP1 v. LC3 + LAMP1,
857 P < 0.0001).

858

859 **Figure 2. JIP3 and JIP4 induce dynein activity *in vitro*. (A)** Schematic illustrating our single-molecule
860 motility assay. **(B)** Example kymographs showing the growth and catastrophe dynamics used to
861 differentiate the plus-end of the microtubule from the more stable minus-end. **(C)** Quantification of the
862 directionality of runs on each microtubule. Runs were defined as events $\geq 0.8\mu\text{m}$ in length towards either
863 the minus- or plus-end of the microtubule (MT). Symbols indicate comparison to the BICD2N dynein
864 positive control. Kruskal-Wallis test with Dunn's multiple comparisons. n = 20 MT each. K560 v. BICD2N,

865 $P < 0.0001$; K560 v. JIP3, $P < 0.0001$; K560 v. JIP4, $P < 0.0001$; BICD2N v. JIP3, $P > 0.9999$; BICD2N
866 v. JIP4, $P > 0.9999$; JIP3 v. JIP4, $P > 0.9999$. **(D-F)** Example kymograph and quantification showing the
867 activity of BICD2N-containing dynein complexes. **(G-I)** Example kymograph and quantification showing
868 the activity of JIP3-containing dynein complexes. **(J-L)** Example kymograph and quantification showing
869 the activity of JIP4-containing dynein complexes. All velocity histograms were fit to a Gaussian curve and
870 all run length histograms (1– cumulative distribution frequency) were fit to a one phase decay. Listed
871 values are median (25th percentile–75th percentile). $n = 97$ – 192 events. Complexes with a net direction of
872 “0” were stationary landing events, while complexes with a net direction of “–” or “+” moved $\geq 0.8 \mu\text{m}$
873 towards the minus- or plus-end of the microtubule respectively. $n = 20$ MT each; Kruskal-Wallis test with
874 Dunn’s multiple comparisons; JIP3 (0 v. –, $P = 0.6412$; 0 v. +, $P = 0.0051$; – v. +, $P < 0.0001$); JIP4 (0 v.
875 –, $P > 0.9999$; 0 v. +, $P = 0.0004$; – v. +, $P < 0.0001$).

876

877 **Figure 3. RAB10 overexpression inhibits retrograde autophagosomal transport. (A)** Example
878 western blot and quantification showing RAB10 in the AV fraction. $n = 4$ preparations; unpaired t test, P
879 $= 0.1308$. **(B-C)** Example kymograph and quantification showing the fraction of LC3 moving retrograde,
880 anterograde, or exhibiting bidirectional/stationary motion in the presence of EGFP alone (Control) or
881 EGFP-RAB10. $n = 9$ neurons; two-way ANOVA with Sidak’s multiple comparisons test (anterograde, P
882 $= 0.7646$; stationary/bidirectional, $P = 0.0166$; retrograde, $P = 0.0013$). **(D)** Within the RAB10-expressing
883 cells, motility of the LC3+ puncta either colocalized with RAB10 (+ RAB10) or not (– RAB10). $n = 9$
884 neurons; two-way ANOVA with Sidak’s multiple comparisons test (anterograde, $P = 0.0897$;
885 stationary/bidirectional, $P = 0.0016$; retrograde, $P = 0.3700$). **(E)** Fraction of autophagosomes (HT-LC3
886 only), autolysosomes (LC3+ LAMP1), or lysosomes (endogenous LAMP1 only) in fixed cells colocalized
887 with EGFP-RAB10. $n = 14$ – 16 neurons; one-way ANOVA with Tukey’s multiple comparisons test (LC3 v.
888 LC3 + LAMP1, $P = 0.0181$; LC3 v. LAMP1, $P = 0.0179$; LAMP1 v. LC3 + LAMP1, $P > 0.9999$). **(F)** Of the
889 EGFP-RAB10 that was colocalized with LC3 and/or LAMP1, fraction colocalized with each organelle
890 type. $n = 14$ – 16 neurons; one-way ANOVA with Tukey’s multiple comparisons test (LC3 v. LC3 + LAMP1,
891 $P = 0.0070$; LC3 v. LAMP1, $P < 0.0001$; LAMP1 v. LC3 + LAMP1, $P = 0.0030$).

892

893 **Figure 4. RAB10 overexpression shifts the lysosomal population towards anterograde motility.**

894 **(A-B)** Quantification and example kymographs showing the fraction of LC3 moving retrograde,
895 anterograde, or exhibiting bidirectional/stationary motion in the presence of EGFP alone (Control) or
896 EGFP-RAB10. n = 14 neurons; two-way ANOVA with Sidak's multiple comparisons test (anterograde, P
897 = 0.8445; stationary/bidirectional, P = 0.7328; retrograde, P = 0.2696). **(C)** Fraction of the motile LAMP1
898 puncta (moving $\leq 10\mu\text{m}$ in either direction during a 2 min video) moving anterograde. n = 14 neurons;
899 unpaired t test (P = 0.0297). **(D)** Within the RAB10-expressing cells, motility of the LAMP1+ puncta either
900 colocalized with RAB10 (+ RAB10) or not (- RAB10). n = 9 neurons; two-way ANOVA with Sidak's
901 multiple comparisons test (anterograde, P = 0.5595; stationary/bidirectional, P = 0.3011; retrograde, P =
902 0.9651).

903

904 **Figure 5. ARF6 regulates the motility of autophagosomes in the axon in a GTP-dependent fashion.**

905 **(A)** Example western blot and quantification showing ARF6 in the AV fraction. n = 4 preparations;
906 unpaired t test, P = 0.0159. **(B)** Schematic illustrating the general characteristics of GTP- or GDP-ARF6
907 and the locked point mutants. **(C-D)** Example kymographs and quantification of mCherry (mCh)-LC3
908 motile fractions under the expression of CFP-ARF6^{WT}, ARF6^{Q67L}, or ARF6^{T27N}. n = 15-18 neurons; two-
909 way ANOVA with Tukey's multiple comparisons; anterograde (WT v. QL, P = 0.9333; WT v. TN, P =
910 0.8377; QL v. TN, P = 0.9795); stationary/bidirectional (WT v. QL, P = 0.0824; WT v. TN, P = 0.0021; QL
911 v. TN, P < 0.0001); retrograde (WT v. QL, P = 0.1723; WT v. TN, P = 0.0003; QL v. TN, P < 0.0001).
912 Symbols indicate comparison to ARF6^{WT}. **(E)** Number of seconds paused per min in each of the three
913 conditions (for all AVs). n = 83-111 puncta; Kruskal-Wallis test with Dunn's multiple comparisons; WT v.
914 QL, P = 0.1526; WT v. TN, P = 0.0327; QL v. TN, P < 0.0001.

915

916 **Figure 6. ARF6 GTP-locked mutant decreases retrograde lysosome pausing. (A-B)** Example

917 kymographs and quantification of LAMP1-HT motile fractions under the expression of CFP-ARF6^{WT},
918 ARF6^{Q67L}, or ARF6^{T27N}. n = 10 neurons; two-way ANOVA with Tukey's multiple comparisons; anterograde

919 (WT v. QL, $P = 0.0428$; WT v. TN, $P = 0.0314$; QL v. TN, $P = 0.9915$); stationary/bidirectional (WT v. QL,
920 $P = 0.0011$; WT v. TN, $P = 0.2466$; QL v. TN, $P = 0.0960$); retrograde (WT v. QL, $P = 0.4213$; WT v. TN,
921 $P = 0.6013$; QL v. TN, $P = 0.0729$). Symbols indicate comparison to ARF6^{WT}. **(C-F)** Number of seconds
922 paused per min in each of the 3 conditions for all LAMP1 puncta (C; $n = 223$ -274 puncta; WT v. QL, $P <$
923 0.0001 ; WT v. TN, $P = 0.0059$; QL v. TN, $P = 0.0001$), LAMP1 with (D; $n = 49$ -67 puncta; WT v. QL, $P =$
924 0.0029 ; WT v. TN, $P > 0.9999$; QL v. TN, $P = 0.0265$) and without LC3 (D; $n = 174$ -206 puncta; WT v.
925 QL, $P < 0.0001$; WT v. TN, $P = 0.0198$; QL v. TN, $P = 0.0431$), and all the retrograde- (E; $n = 49$ -65
926 puncta; WT v. QL, $P = 0.0004$; WT v. TN, $P = 0.6390$; QL v. TN, $P = 0.0574$) or anterograde- (E; $n = 27$ -
927 73 puncta; WT v. QL, $P = 0.0507$; WT v. TN, $P > 0.9999$; QL v. TN, $P = 0.0846$) moving LAMP1 puncta.
928 Kruskal-Wallis test with Dunn's multiple comparisons.

929

930 **Figure 7. ARF6 GEFs are enriched on the outer AV membrane and may act to locally enrich ARF6-**
931 **GTP. (A)** Schematic illustrating the GAP-GEF cycle for small GTPases. **(B)** Relative enrichment
932 (normalized number of peptides, see Methods for details) for ARF6 GEFs and GAPs in the proteomics
933 performed by Goldsmith et al., (2022) and Dumrongprechachan et al., (2022). All of the known ARF6
934 GEFs and GAPs that were detected in either organelle enrichment are listed in the figure. Note that some
935 ARF6 GAPs/GEFs were not found in either enrichment [EFA6A-D (GEFs), GIT2 (GAP), ADAP1 (GAP),
936 ACAP1,3 (GAP), ASAP3 (GAP), ARAP1,3 (GAP)]. **(C)** Example western blot and **(D-G)** quantification
937 showing GEF enrichment in the AV fraction. **(H)** Example western blot and **(I-K)** quantification showing
938 GAPs in the AV fraction. $n = 4$ preparations; unpaired t test; (D) $P = 0.0139$; (E) $P = 0.0038$; (F) $P =$
939 0.0701 ; (G) $P = 0.0050$; (I) $P = 0.1549$; (J) $P = 0.3208$; (K) $P = 0.7078$.

940

941 **Figure 8. ARF6 induces the recruitment of JIP3/4 to microtubules. (A)** Example kymographs showing
942 the activity of JIP3- and JIP4- containing complexes in the presence of CFP-ARF6^{Q67L}. **(B-C)**
943 Quantification of the number of total landing events for JIP3- and JIP4-containing complexes in the
944 presence or absence of CFP-Arf6^{Q67L}. $n = 20$ MT each; unpaired t test; JIP3, $P < 0.0001$; JIP4, $P =$
945 0.0011 . **(D-E)** Number of events (per μm microtubule per min) observed for JIP3-containing and JIP4-

946 containing complexes, either in the presence or absence of ARF6^{Q67L}. Complexes with a net direction of
947 “0” were stationary landing events, while complexes with a net direction of “-” or “+” moved $\geq 0.8 \mu\text{m}$
948 towards the minus- or plus-end of the microtubule respectively. Note that the -ARF6 data from is repeated
949 from Figure 2. Kruskal-Wallis test with Dunn’s multiple comparisons. n = 20 MT each. JIP3 -ARF6 v. +
950 ARF6: 0, P < 0.0001; -, P > 0.9999; +, P > 0.9999. JIP4 -ARF6 v. + ARF6: 0, P = 0.0033; -, P > 0.9999;
951 +, P > 0.9999.

952

953 **Figure 9. Integrated model of autophagosome, autolysosome, and lysosome transport along**
954 **axons. (A)** We demonstrate that the GTP-bound ARF6 is enriched on AV membranes, where it can
955 recruit its interacting partners JIP3 or JIP4. JIP3/4 can then recruit dynactin and dynein and activate
956 minus-end-directed retrograde motility especially of autolysosomes. By contrast, we propose that ARF6
957 is removed from the lysosomal membrane by local ARF6 GAP activity, which may be promoted by the
958 presence of phosphorylated RABs, including RAB10. RAB10 plays an unknown role in transport, but
959 seems to induce anterograde transit, possibly through a JIP3- or JIP4-JIP1-kinesin-1 complex. These
960 motor complexes are not the only ones involved in AV or lysosome transport; we highlight a few
961 complementary complexes on the left. **(B)** One mechanism by which this pathway may be disrupted in
962 neurodegeneration is via hyperphosphorylation of RABs. The disease-causing mutations in LRRK2
963 kinase result in increased phospho-RABs and also increased recruitment of kinesin-1 to the AV
964 membrane. However, the resulting loss of AV motility can be rescued by expressing GTP-locked ARF6;
965 thus these motor-regulatory mechanisms are interconnected and possibly competitive.

966 **Supplement legends**

967 **Figure S1. JIP3 or JIP4 overexpression does not affect AV or lysosome transport. (A-C)** Example
968 kymographs showing LC3 and LAMP1 puncta motile behavior in the axons of neurons expressing
969 HaloTag (HT) alone (Tag), HT-JIP3, or HT-JIP4. Annotated kymographs (annot.) show paths pseudo-
970 colored for visualization; heavier weight lines represent paths with both LC3 and LAMP1 co-migrating.
971 **(D-E)** Quantification of the fraction of LC3 or LAMP1 puncta moving retrograde ($\geq 10\mu\text{m}$ towards the
972 soma), anterograde ($\geq 10\mu\text{m}$ towards the axon tip), or exhibiting bidirectional/stationary motility (moving
973 $< 10\mu\text{m}$). Symbols indicate comparison to Tag; $n = 15$ neurons; two-way ANOVA with Tukey's multiple
974 comparisons test; LC3 [variation between motile fractions ($P < 0.0001$) but no variation between
975 conditions ($P > 0.9999$) nor interaction ($P = 0.4514$)]; LAMP1 [variation between motile fractions ($P <$
976 0.0001) and mild interaction ($P = 0.0032$) but no variation between conditions ($P > 0.9999$)]. **(F-G)** LC3
977 and LAMP1 puncta density (per μm in a 2 min video) in cells expression HT-JIP3, HT-JIP4, or Tag. $n =$
978 11-15 neurons; one-way ANOVA with Tukey's multiple comparisons test (LC3, $P = 0.9076$; LAMP1, $P =$
979 0.9397). **(H-I)** Colocalization between LC3 and LAMP1 puncta in cells expression HT-JIP3, HT-JIP4, or
980 Tag. $n = 11-15$ neurons; one-way ANOVA with Tukey's multiple comparisons test (LC3, $P = 0.3154$;
981 LAMP1, $P = 0.5569$). **(J-K)** Western blot and quantification demonstrating that HT-JIP3 or JIP4 in the
982 CMV backbone expresses far more highly than in the EGFP backbone (EGFP sequence has been
983 removed by subcloning). This experiment was performed using COS-7 cells, which we transfected at the
984 same confluence ($\sim 50\%$) with FuGene and equal DNA quantities. After lysis in RIPA buffer, we assessed
985 for protein concentration using BCA assay. Equal protein concentrations were loaded, which was
986 confirmed using Revert Total Protein Stain. Finally, a monoclonal HT antibody was used to assess
987 expression of the HT proteins. $n = 3$; one-way ANOVA with Sidak's multiple comparisons test (JIP3 EGFP
988 v. JIP3 CMV, $P = 0.0051$; JIP4 EGFP v. JIP4 CMV, $P = 0.0444$; JIP3 EGFP v. JIP4 EGFP, $P = 0.9118$;
989 JIP3 CMV v. JIP4 CMV, $P = 0.0857$). **(L)** Example PLA negative (Neg.) control (missing JIP3/4 antibody).
990 **(M)** Quantification of DIC PLA puncta either with JIP3, JIP4, or no second 1^o antibody (Neg. control). $n =$
991 20-21 neurons; one-way ANOVA with Tukey's multiple comparisons test (JIP3 v. JIP4, $P = 0.6763$; JIP3
992 v. Neg., $P < 0.0001$; JIP4 v. Neg., $P < 0.0001$).

993

994 **Figure S2. JIP3 and JIP4 do not induce kinesin activity *in vitro*.** (A) Example kymograph of labeled
995 KIF5C¹⁻⁵⁶⁰ (K560) activity. (B) Number of events (per μm microtubule per min) observed for K560-
996 containing complexes. $n = 20$ MT each; Kruskal-Wallis test with Dunn's multiple comparisons; K560: 0 v.
997 -, $P = 0.0004$; 0 v. +, $P = 0.3092$; - v. +, $P < 0.0001$. (C-E) Quantification of velocities and run lengths
998 towards the MT plus end for K560-, JIP3-, or JIP4-containing complexes. All velocity histograms were fit
999 to a Gaussian curve and all run length histograms (1- cumulative distribution frequency) were fit to a one
1000 phase decay. Listed values are median (25th percentile-75th percentile). JIP3/JIP4, $n = 19-22$ events;
1001 K560, $n = 160$ events. (F-G) Quantification of the directionality of runs on each microtubule. Runs were
1002 defined as events $\geq 0.8 \mu\text{m}$ in length towards either the minus- or plus-end of the microtubule. Note that
1003 the + LIS1 and - KIF5C & KLC2 are repeated from Figure 2. $n = 15-20$ MT each; Kruskal-Wallis test with
1004 Dunn's multiple comparisons; LIS1: JIP3 $P > 0.9999$, JIP4 $P > 0.9999$; KIF5&KLC: JIP3 $P = 0.3572$, JIP4
1005 $P > 0.9999$.

1006

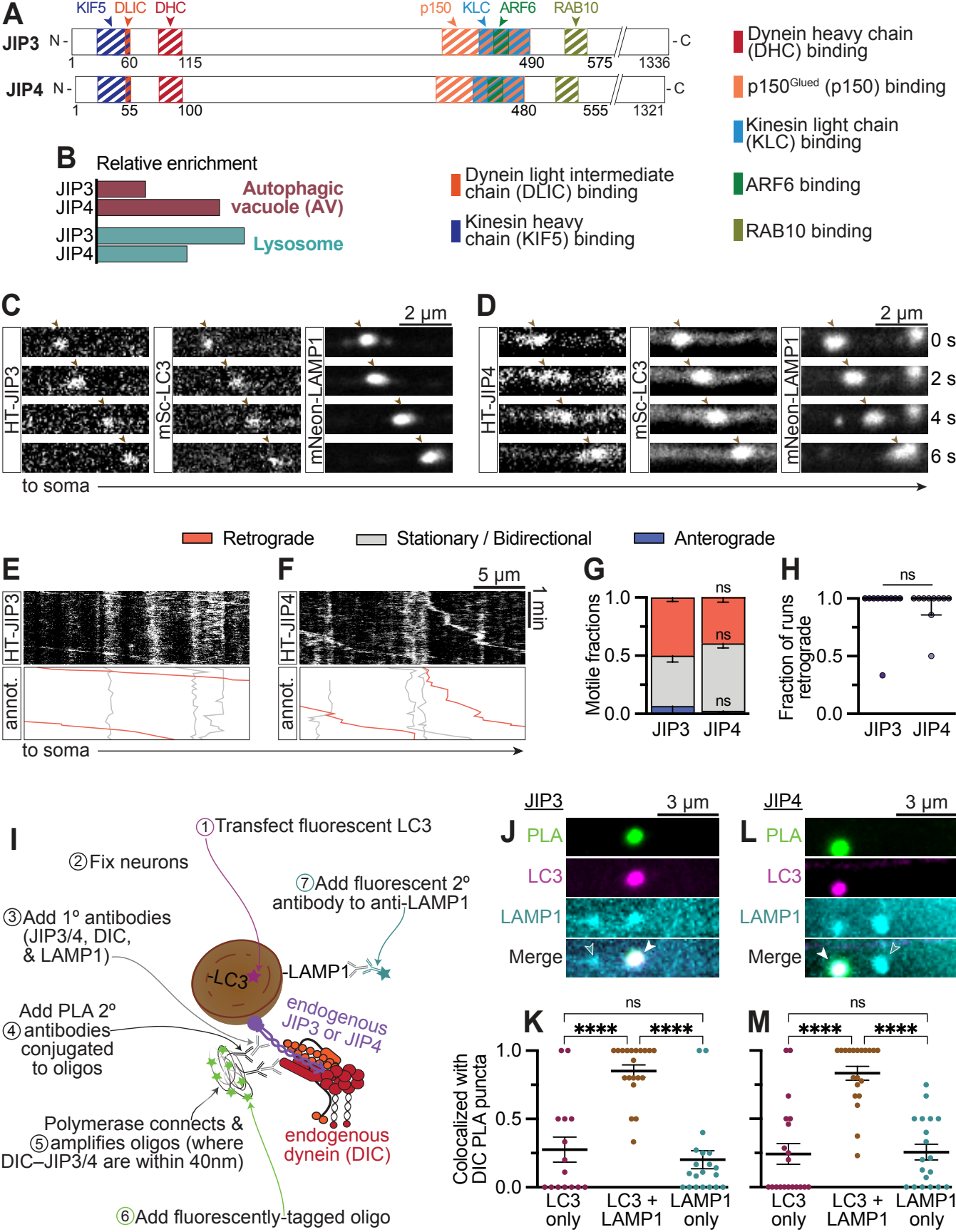
1007 **Figure S3. RAB10 expression does not affect the formation of JIP3/4-dynein complexes.** (A-B)
1008 Quantification of mSc-LC3 puncta linear density and colocalization with LAMP1-HT. $n = 9$ neurons;
1009 unpaired t test; density, $P = 0.7068$; colocalization, $P = 0.3086$. (C-D) Quantification of LAMP1-HT puncta
1010 linear density and colocalization with mSc-LC3. $n = 9$ neurons; unpaired t test; density, $P = 0.0438$;
1011 colocalization, $P = 0.8564$. (E-F) Total JIP3- or JIP4-DIC PLA puncta linear density, compared between
1012 cells expressing EGFP alone (Tag) and cells expressing EGFP-RAB10. Note that the Tag data is
1013 repeated from Fig. S1 M. $n = 20$ neurons; unpaired t test; JIP3, $P = 0.3278$; JIP4, $P = 0.5541$. (G-H)
1014 Colocalization between JIP3/4-DIC PLA puncta and AVs or lysosomes. Note that Note that the Tag data
1015 is repeated from Fig. 1 K, M. $n = 20$ neurons; one-way ANOVA with Tukey's multiple comparisons test;
1016 JIP3 (LC3 only, $P = 0.7989$; LC3 + LAMP1, $P = 0.9971$; LAMP1 only, $P = 0.7486$); JIP4 (LC3 only, $P =$
1017 0.9984 ; LC3 + LAMP1, $P = 0.2160$; LAMP1 only, $P > 0.9999$).

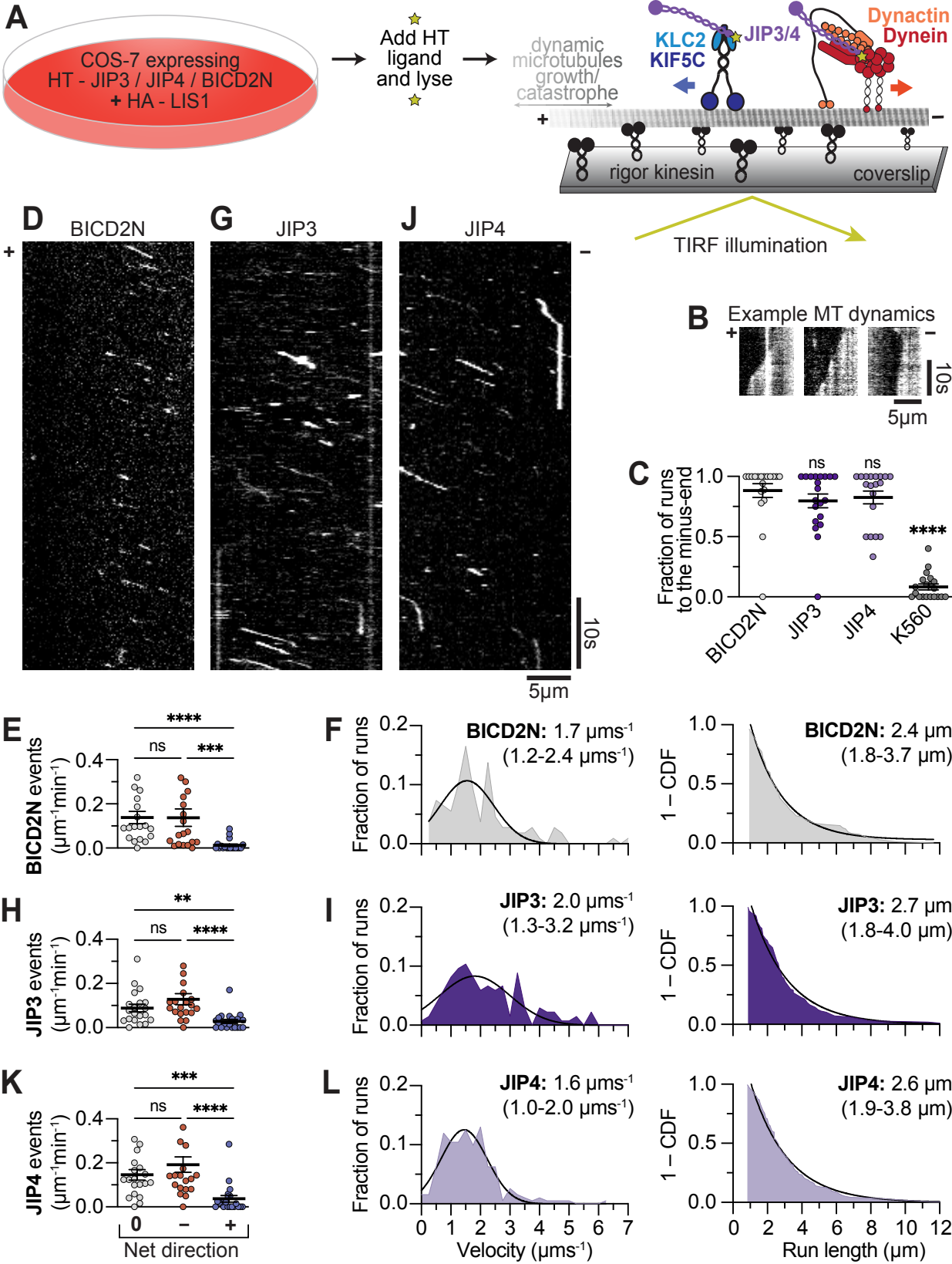
1018

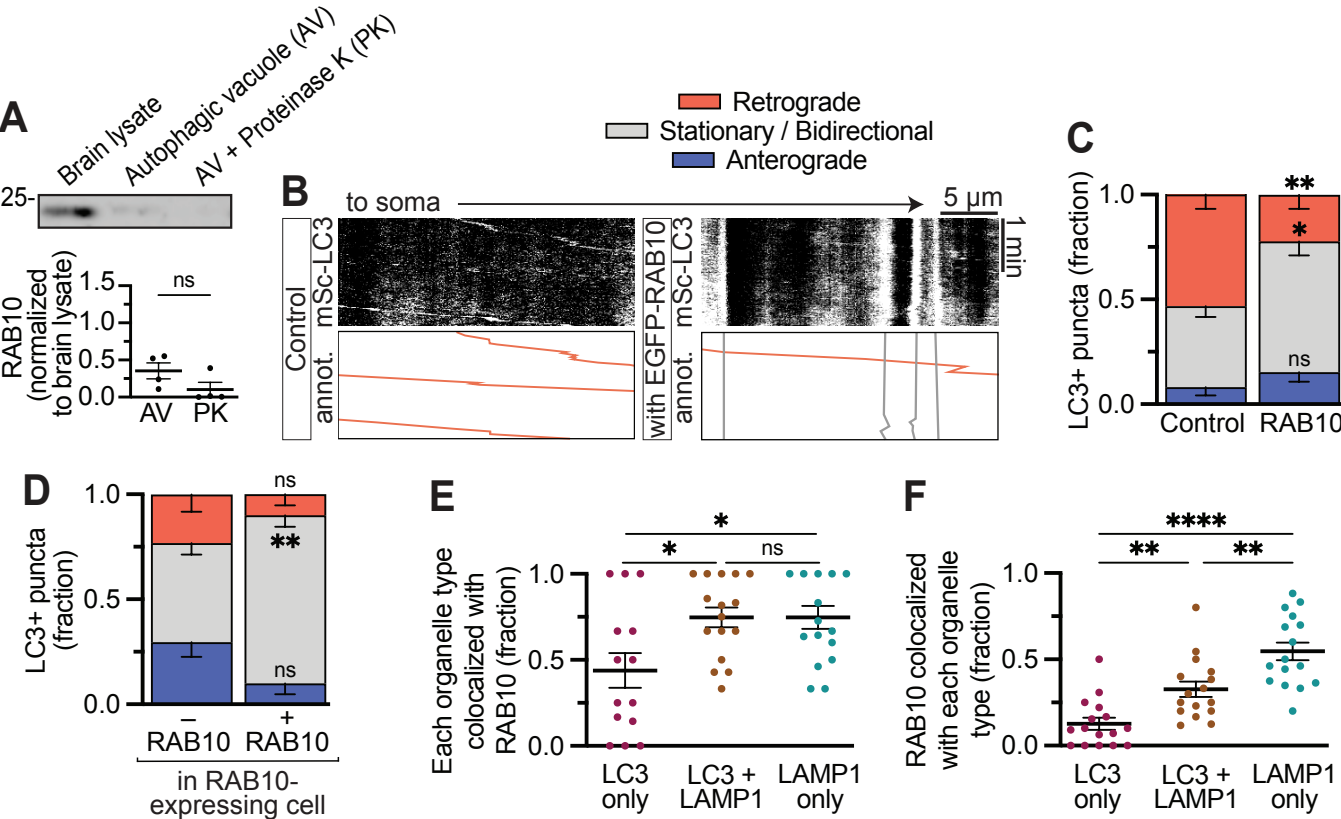
1019 **Figure S4. ARF6 expression does not affect LC3 or LAMP1 density or colocalization. (A)**
1020 Quantification of mCh-LC3 puncta linear density. n = 13-16 neurons; one-way ANOVA with Sidak's
1021 multiple comparisons test; WT v. QL, P = 0.6382; WT v. TN, P = 0.8339; QL v. TN, P = 0.6382. **(B)**
1022 Quantification of mCh-LC3 colocalization with LAMP1-HT. one-way ANOVA with Sidak's multiple
1023 comparisons test; n = 9-11 neurons; WT v. QL, P = 0.4183; WT v. TN, P = 0.9791; QL v. TN, P = 0.4183.
1024 **(C)** Quantification of LC3 non-processive movement, as described by Δ run length (net run length of each
1025 vesicle subtracted from its total run displacement). n = 71-111 puncta; Kruskal-Wallis test with Dunn's
1026 multiple comparisons test; WT v. QL, P > 0.9999; WT v. TN, P > 0.9999; QL v. TN, P > 0.9999. **(D)**
1027 Quantification of LAMP1-HT puncta linear density. one-way ANOVA with Sidak's multiple comparisons
1028 test; n = 10 neurons; WT v. QL, P = 0.1665; WT v. TN, P = 0.6735; QL v. TN, P = 0.2495. **(E)**
1029 Quantification of LAMP1-HT colocalization with mCh-LC3. one-way ANOVA with Sidak's multiple
1030 comparisons test; n = 10 neurons; WT v. QL, P = 0.6020; WT v. TN, P = 0.5742; QL v. TN, P = 0.3846.
1031 **(F)** Quantification of LAMP1 non-processive movement, as described by Δ run length. n = 13-16 neurons;
1032 Kruskal-Wallis test with Dunn's multiple comparisons test; WT v. QL, P > 0.9999; WT v. TN, P > 0.9999;
1033 QL v. TN, P > 0.9999.

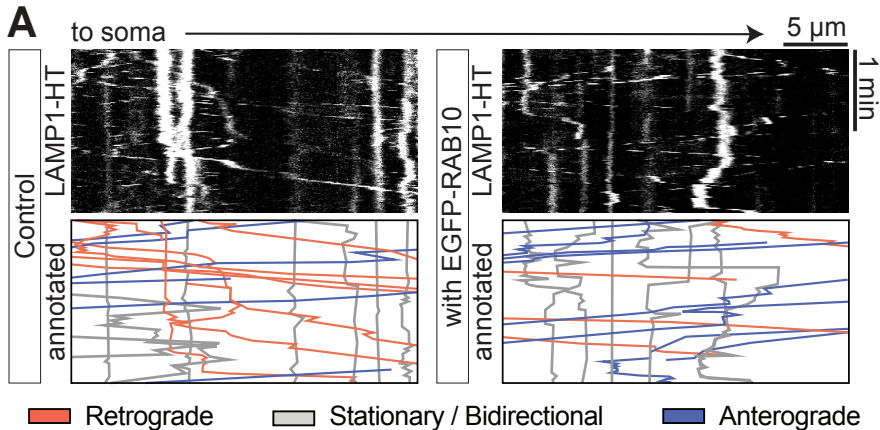
1034
1035 **Figure S5. ARF6 does not affect motile events *in vitro*. (A)** Example kymographs showing the activity
1036 of JIP3- and JIP4- containing complexes in the presence of CFP-ARF6^{T27N}. **(B-C)** Quantification of the
1037 number of total landing events for JIP3- and JIP4-containing complexes in the presence of CFP-Arf6^{Q67L}
1038 or CFP-Arf6^{T27N}. n = 20-23 MT each; unpaired t test; JIP3, P < 0.6856; JIP4, P = 0.1028. **(D-E)** Number
1039 of events (per μ m microtubule per min) observed for JIP3-containing and JIP4-containing complexes in
1040 the presence of CFP-Arf6^{Q67L} or CFP-Arf6^{T27N}. Complexes with a net direction of "0" were stationary
1041 landing events, while complexes with a net direction of "-" or "+" moved $\geq 0.8 \mu$ m towards the minus- or
1042 plus-end of the microtubule respectively. Note that the Arf6^{QL} data from is repeated from Figure 8.
1043 Kruskal-Wallis test with Dunn's multiple comparisons. n = 20-23 MT each. JIP3 QL v. TN: 0, > 0.9999; -
1044 , P > 0.9999; +, P > 0.9999. JIP4 QL v. TN: 0, 0, > 0.9999; -, P = 0.9389; +, P > 0.9999. Dashed lines
1045 indicate mean without added ARF6. **(F)** Quantification of the activity of JIP3 or JIP4-containing dynein

1046 complexes in the presence of CFP-Arf6^{Q67L}. **(G)** Quantification of the activity of JIP3 or JIP4-containing
1047 kinesin complexes in the presence of CFP-Arf6^{Q67L}. All velocity histograms were fit to a Gaussian curve
1048 and all run length histograms (1– cumulative distribution frequency) were fit to a one phase decay. Listed
1049 values are median (25th percentile-75th percentile). n = 39-140 events.









— Retrograde

— Stationary / Bidirectional

— Anterograde

